Radiation mechanisms and geometry of Cygnus X-1 in the soft state

Marek Gierliński,[1,2] Andrzej A. Zdziarski,[2] Juri Poutanen,[3] Paolo S. Coppi,[4] Ken Ebisawa[5] and W. Neil Johnson[6]

[1]*Astronomical Observatory, Jagiellonian University, Orla 171, 30-244 Cracow, Poland*
[2]*N. Copernicus Astronomical Center, Bartycka 18, 00-716 Warsaw, Poland*
[3]*Stockholm Observatory, SE-133 36 Saltsjöbaden, Sweden*
[4]*Astronomy Department, Yale University, PO Box 208101, New Haven, CT 062520-8101, USA*
[5]*Code 660.2, Laboratory for High Energy Astrophysics, NASA/Goddard Space Flight Center, Greenbelt, MD 20771, USA*
(also at Universities Space Research Association)
[6]*E. O. Hulbert Center for Space Research, Naval Research Laboratory, Washington, DC 20375, USA*

ABSTRACT

We present X-ray/γ-ray spectra of Cyg X-1 observed during the transition from the hard to the soft state and in the soft state by *ASCA*, *RXTE* and *CGRO*/OSSE in 1996 May and June. The spectra consist of a dominant soft component below ~ 2 keV and a power-law-like continuum extending to at least ~ 800 keV. We interpret them as emission from an optically thick, cold accretion disc and from an optically thin, non-thermal corona above the disc. A fraction $f \gtrsim 0.5$ of total available power is dissipated in the corona.

We model the soft component by multicolour blackbody disc emission taking into account the torque-free inner-boundary condition. If the disc extends down to the minimum stable orbit, the *ASCA/RXTE* data yield the most probable black hole mass of $M_X \approx 10 \, M_\odot$ and an accretion rate, $\dot{M} \approx 0.5 L_E/c^2$, locating Cyg X-1 in the soft state in the upper part of the stable, gas-pressure-dominated, accretion-disc solution branch.

The spectrum of the corona is well modelled by repeated Compton scattering of seed photons from the disc off electrons with a hybrid, thermal/non-thermal distribution. The electron distribution can be characterized by a Maxwellian with an equilibrium temperature of $kT_e \sim 30$–50 keV, a Thomson optical depth of $\tau \sim 0.3$ and a quasi-power-law tail. The compactness of the corona is $2 \lesssim \ell_h \lesssim 7$, and a presence of a significant population of electron–positron pairs is ruled out.

We find strong signatures of Compton reflection from a cold and ionized medium, presumably an accretion disc, with an apparent reflector solid angle, $\Omega/2\pi \sim 0.5$–0.7. The reflected continuum is accompanied by a broad iron Kα line.

Key words: accretion, accretion discs – radiation mechanisms: non-thermal – stars: individual: Cygnus X-1 – gamma-rays: observations – gamma-rays: theory – X-rays: stars.

1 INTRODUCTION

Cyg X-1 is the best-studied Galactic black hole candidate. Its X-ray source was discovered in a 1964 June rocket flight (Bowyer et al. 1965). Its optical companion is HDE 226868 (Bolton 1972; Webster & Murdin 1972), an OB supergiant (Walborn 1973). HDE 226868 belongs to the NGC 6871/Cyg OB3 association (Massey, Johnson & DeGioia-Eastwood 1995). The distance to the association has been measured by Massey et al. to be $D \approx 2.1 \pm 0.1$ kpc, whereas Malysheva (1997) obtained $D \approx 1.8$ kpc using a different photometric system. Hereafter, we adopt $D = 2$ kpc. We note that a commonly used value of 2.5 kpc was obtained from the lower limit set by the extinction observed towards Cyg X-1

compared to the extinction–distance dependence for stars with directions close to that of Cyg X-1 (Bregman et al. 1973; Margon, Bowyer & Stone 1973). However, this method cannot be used for OB supergiants, in which case a significant part of the extinction is commonly local (e.g. Massey et al. 1995).

The spectroscopic mass function is

$$f_M = \frac{M_X \sin^3 i}{(1 + M_O/M_X)^2} = (0.252 \pm 0.010) \, M_\odot \tag{1}$$

(Gies & Bolton 1982), where i is the inclination of the orbital axis to the observer, and M_O and M_X are the masses of the supergiant and the compact object, respectively. The mass ratio, $q \equiv M_O/M_X$,
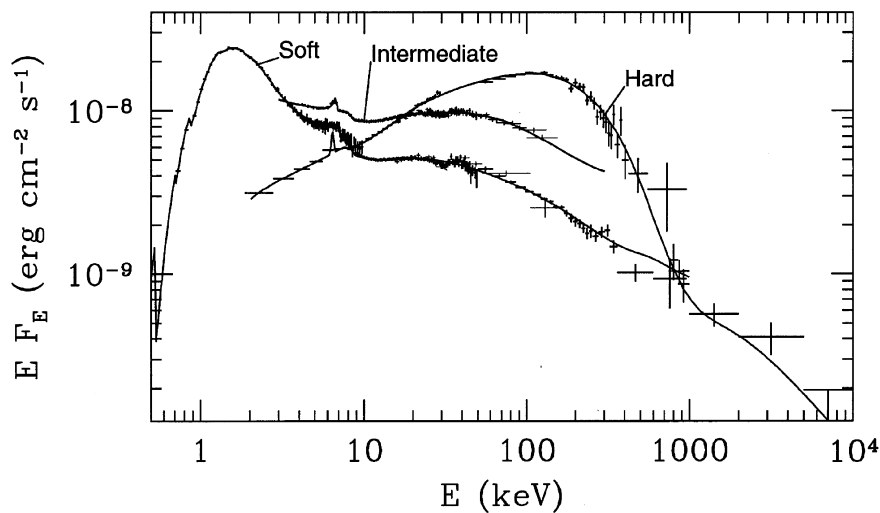
Figure 1. Spectral states of Cyg X-1. The hard-state spectrum was observed by *Ginga* and OSSE on 1991 June 6 (G97) and by COMPTEL 1991 May 30–June 8 (McConnell et al. 1994). The intermediate state was observed by *RXTE* on 1996 May 23 (data set 2 in Table 1). The soft state was observed by *ASCA* and *RXTE* on 1996 May 30 (data set 3) and by OSSE 1996 June 14–25 (data set 10). Here and in subsequent figures, the spectral data are re-binned for clarity. The curves correspond to the hybrid model described in Section 3.4.

has been constrained to be within $1.5 \lesssim q \lesssim 2.3$ (Gies & Bolton 1986; Ninkov, Walker & Yang 1987). Thus M_X is strongly anticorrelated with i,

$$1.5\,M_\odot \lesssim M_X \sin^3 i \lesssim 2.9\,M_\odot. \qquad (2)$$

The companion mass, M_O, is probably in a range between $\sim 15\,M_\odot$ (Herrero et al. 1995) and $\sim 30\,M_\odot$ (Gies & Bolton 1986). This mass range together with the above range of q lead to M_X between ~ 6.5 and $\sim 20\,M_\odot$. Combined with the mass function, these constraints imply $25° \lesssim i \lesssim 50°$. This is within limits from various considerations (e.g. Davis & Hartman 1983; Ninkov et al. 1987; Dolan & Tapia 1989) yielding $25° \lesssim i \lesssim 67°$ (where the upper limit is due to the lack of eclipses), and a recent Hα Doppler tomography (Sowers et al. 1998), giving $i \lesssim 55°$.

The X-ray/γ-ray (hereafter Xγ) emission of Cyg X-1 undergoes transitions between a hard (also called 'low') spectral state and a soft ('high') one. Most of the time the source is in the hard state, where the Xγ spectrum can be roughly described by a hard power law with a photon index of $\Gamma \sim 1.6$–1.8 and a high-energy cut-off above $\sim 100\,\mathrm{keV}$, and a Compton reflection component including an Fe Kα line (e.g. Gierliński et al. 1997a, hereafter G97). A soft excess observed below $\sim 3\,\mathrm{keV}$ includes a blackbody with temperature $kT_{\mathrm{bb}} \sim 0.15\,\mathrm{keV}$ (Bałucińska-Church et al. 1995; Ebisawa et al. 1996). A likely model for the hard state of Cyg X-1 embodies Comptonization of blackbody photons from an optically thick accretion disc in a hot, thermal, optically thin plasma.

In the soft state, the Xγ spectrum is dominated by a soft, blackbody-like component peaking at $\sim 1\,\mathrm{keV}$ followed by a tail, which can be roughly described as a power law with $\Gamma \sim 2.5$ (Dolan et al. 1977; Ogawara et al. 1982), extending to at least several hundred keV (Phlips et al. 1996). The soft component can be modelled as thermal emission from an optically thick accretion disc (Mitsuda et al. 1984; Hanawa 1989). The nature of the hard tail has remained unclear. The soft state of Cyg X-1 was observed in 1970, 1975, 1980, 1994 and 1996, each time lasting no more than a few months (Liang & Nolan 1984; Cui et al. 1997). In 1994, the soft state was observed only in hard X-rays and soft γ-rays by the OSSE and BATSE detectors aboard *Compton Gamma Ray*
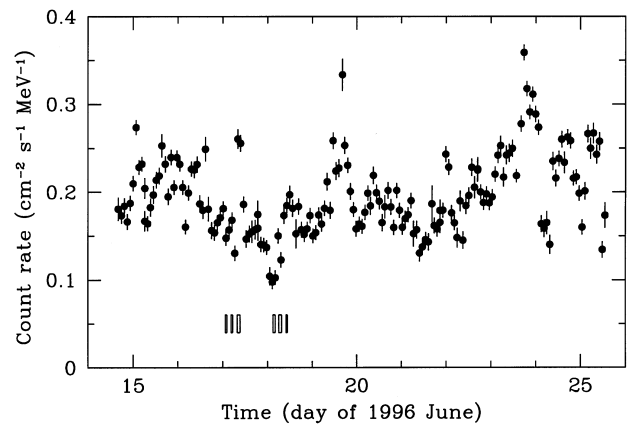

Figure 2. The OSSE light-curve in the 50–150 keV band. Each data point corresponds to one orbit. The boxes in the lower part of the plot indicate the times of six *RXTE* observations (Nos. 4–9 in Table 1).

Observatory (Phlips et al. 1996; Ling et al. 1997; Paciesas et al. 1997), with no accompanying observations in soft X-rays. Fig. 1 shows Xγ spectra of Cyg X-1 in the hard and soft states of 1991 and 1996, respectively, as well as in an intermediate state of 1996 May.

In this paper we study *RXTE*, *ASCA* and OSSE spectral data from observations of Cyg X-1 during its soft state in 1996. We find that spectra can be well described by emission of a non-thermal plasma in the vicinity of an accretion disc. We then study implications of this model for the size of the plasma and its location with respect to the disc, the presence of e^+e^- pairs, the inner radius of the accretion disc, the disc stability, and the mass of the central black hole.

2 THE DATA

The soft state of 1996 lasted approximately from May 16 to August 11 (Zhang et al. 1997c). The observation log of *RXTE* and OSSE observations is given in Table 1.

The *RXTE* data, from the HEASARC public archive, were

Table 1. Log of the *RXTE* and OSSE observations. The *ASCA* observation, near-simultaneous with the *RXTE* observation 3, is described in Section 2.

No.	Date (1996)	Time [UT]	PCA Exposure [s]	Count rate [s^{-1}] (4–50 keV)	Time [UT]	HEXTE Exposure [s]	Count rate [s^{-1}] (15–200 keV)	Time [UT]	OSSE Exposure^a [s]	Count rate [s^{-1}] (50–1000 keV)
1	May 22	19:05:21–19:47:45	2176	7437 ± 34	17:58:41–18:17:53	815	253.7 ± 1.9			
2	May 23	14:28:17–15:05:05	1792	6929 ± 29	14:28:33–14:53:05	1136	319.7 ± 1.5			
3	May 30	07:57:53–08:35:29	1872	4796 ± 22	07:57:37–08:18:25	850	163.3 ± 1.6			
4	June 17	01:45:37–01:54:25	544	3357 ± 17	01:45:21–01:54:57	1062	77.8 ± 2.2	01:25:06–02:08:47	4496	8.25 ± 0.61
5	June 17	04:57:53–05:16:17	992	5113 ± 25	05:00:01–05:17:05	647	117.4 ± 1.8	04:30:47–05:16:40	4598	7.52 ± 0.63
6	June 17	08:09:53–08:42:25	816	6309 ± 31	08:09:53–08:42:57	1061	175.1 ± 1.7	07:47:23–09:12:52	3108	11.85 ± 0.77
7	June 18	03:23:13–03:34:25	688	2893 ± 15	03:22:57–03:34:41	510	65.6 ± 2.0	02:52:42–04:04:47	2670	5.79 ± 0.81
8	June 18	06:47:45–07:00:17	768	2859 ± 14	06:38:41–07:01:05	709	54.0 ± 1.9	06:04:56–07:30:08	3506	5.96 ± 0.71
9	June 18	09:59:45–10:25:21	1360	6011 ± 29	09:59:45–10:25:53	1140	140.9 ± 1.6	10:00:15–10:41:46	4235	8.59 ± 0.64
10	June 14–25							15:55:58–13:13:20^b	670501	9.833 ± 0.098

^{a}The sum of two individual detectors live times.
^{b}The start and end time on June 14 and 25, respectively.

Table 2. The fit results of the non-thermal model to the data. Values in parenthesis denote parameters fixed during the fits. Other important fixed parameters are $\ell_s = 10$, $\gamma_{min} = 1.3$, $i = 45°$ and $A_{Fe} = 1.0$. See Section 3.8 for discussion of the fitted values of M_X.

Obs.	N_H (10^{21} cm^{-2})	kT_{max} (eV)	M_X (M$_\odot$)	ℓ_{nth}/ℓ_h	ℓ_h/ℓ_s	τ_i	Γ_{inj}	$\Omega/2\pi$	ξ (erg cm s^{-1})	E_{line} (keV)	EW (eV)	χ^2/d.o.f.
1	(5.0)	(300)	$14.7^{+1.8}_{-1.1}$	(1.0)	$1.04^{+0.16}_{-0.21}$	$2.35^{+0.21}_{-0.33}$	$2.54^{+0.09}_{-0.08}$	$0.24^{+0.05}_{-0.04}$	8700^{+5900}_{-5000}	$6.52^{+0.19}_{-0.20}$	150^{+50}_{-50}	478.5/422
2	(5.0)	(300)	$11.4^{+0.7}_{-0.7}$	(1.0)	$1.60^{+0.12}_{-0.20}$	$1.55^{+0.10}_{-0.16}$	$2.61^{+0.02}_{-0.03}$	$0.30^{+0.04}_{-0.03}$	780^{+390}_{-210}	$6.44^{+0.24}_{-0.25}$	120^{+40}_{-40}	393.2/422
3	$5.2^{+0.1}_{-0.2}$	350^{+8}_{-9}	$13.3^{+1.0}_{-0.8}$	$0.77^{+0.05}_{-0.04}$	$0.36^{+0.01}_{-0.02}$	$0.25^{+0.05}_{-0.04}$	$2.54^{+0.11}_{-0.07}$	$0.63^{+0.13}_{-0.11}$	350^{+250}_{-120}	$6.37^{+0.14}_{-0.14}$	120^{+50}_{-50}	618.2/574
4	(5.0)	480^{+110}_{-70}	$5.6^{+3.9}_{-2.7}$	(1.0)	$0.27^{+0.08}_{-0.04}$	(0.25)	$2.96^{+0.06}_{-0.07}$	$0.60^{+0.12}_{-0.14}$	460^{+2520}_{-270}	$6.43^{+0.19}_{-0.21}$	170^{+60}_{-60}	423.9/476
5	(5.0)	470^{+120}_{-60}	$7.0^{+4.2}_{-3.5}$	(1.0)	$0.27^{+0.08}_{-0.04}$	(0.25)	$3.30^{+0.03}_{-0.05}$	$0.67^{+0.11}_{-0.10}$	450^{+480}_{-130}	$6.41^{+0.20}_{-0.21}$	160^{+50}_{-60}	515.5/476
6	(5.0)	470^{+60}_{-30}	$7.4^{+2.7}_{-2.6}$	(1.0)	$0.26^{+0.04}_{-0.02}$	(0.25)	$3.33^{+0.08}_{-0.04}$	$0.73^{+0.09}_{-0.09}$	410^{+190}_{-110}	$6.30^{+0.09}_{-0.10}$	140^{+50}_{-50}	614.8/476
7	(5.0)	520^{+90}_{-50}	$4.0^{+1.9}_{-1.6}$	(1.0)	$0.30^{+0.07}_{-0.06}$	(0.25)	$2.87^{+0.08}_{-0.08}$	$0.62^{+0.13}_{-0.13}$	460^{+620}_{-240}	$6.48^{+0.08}_{-0.18}$	190^{+60}_{-60}	504.7/476
8	(5.0)	490^{+100}_{-60}	$5.0^{+2.0}_{-2.0}$	(1.0)	$0.25^{+0.08}_{-0.05}$	(0.25)	$2.96^{+0.09}_{-0.08}$	$0.60^{+0.14}_{-0.08}$	590^{+2720}_{-280}	$6.49^{+0.18}_{-0.19}$	180^{+60}_{-30}	610.2/476
9	(5.0)	440^{+150}_{-30}	$9.1^{+3.0}_{-5.0}$	(1.0)	$0.26^{+0.02}_{-0.02}$	(0.25)	$3.43^{+0.05}_{-0.02}$	$0.67^{+0.09}_{-0.08}$	510^{+230}_{-60}	$6.40^{+0.21}_{-0.20}$	140^{+50}_{-50}	549.5/476

obtained during observations with proposal numbers 10412 and 10512. After preliminary selection, we analysed the data of 1996 May 22, 23, 30, and June 17, 18. During the reduction, we rejected data affected by the South Atlantic Anomaly and those for which elevation above Earth's horizon was less then 10°. We then constructed PCA pulse-height spectra, summing up counts from all PCA layers and detectors. We obtained HEXTE spectra separately for cluster A and B. We added a 2 per cent systematic
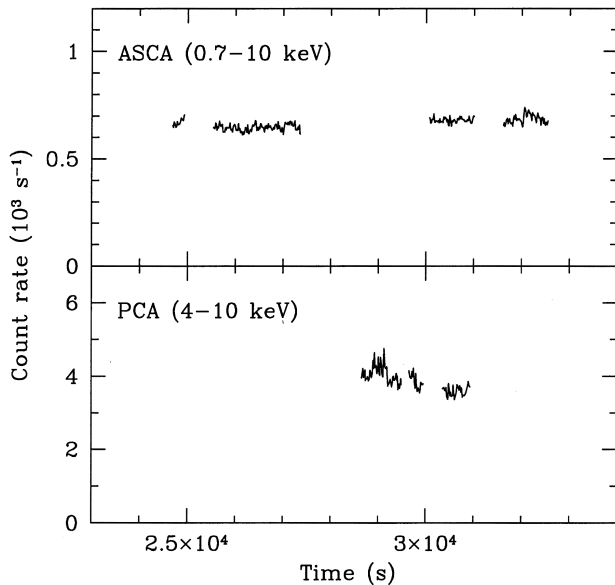

Figure 3. The 0.7–10 keV *ASCA*/GIS and 4–10 keV *RXTE*/PCA light-curves (time is measured from the beginning of 1996 May 30) of the nearly simultaneous observations used here (data set 3 in Table 1).
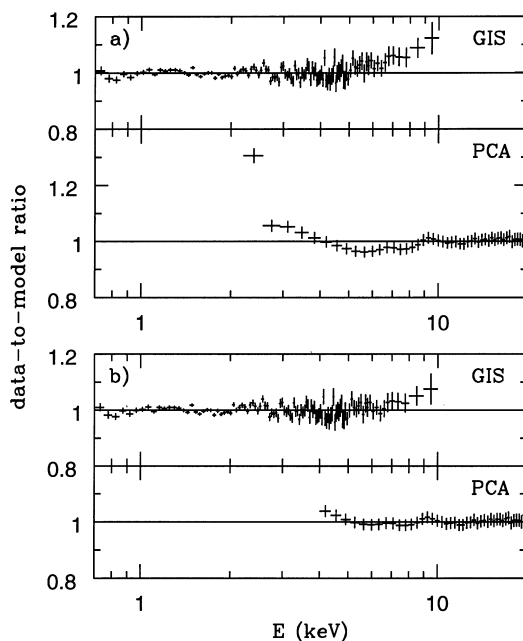

Figure 4. The best fit of the non-thermal model to the near-simultaneous *ASCA* and *RXTE* data of May 30 (observation 3). The upper and lower panels show the data-to-model ratios for *ASCA*/GIS and *RXTE*/PCA, respectively. (a) 0.7–20 keV residuals of the joint fit to the 0.7–10 keV *ASCA* data and the 2–50 keV PCA data. (b) The residuals to the fit with the PCA data restricted to the 4–50 keV range. Note a resulting significant improvement of the joint fit.

error to each PCA channel to represent residual uncertainties of calibration. Since dead-time effects of HEXTE clusters are not yet well established, we allowed free normalization of the HEXTE spectra during spectral fits. We used the PCA response matrices v3.0 as included in the FTOOLS v4.1 released on 1998 May 8, and the HEXTE response matrices of 1997 March 20.

OSSE observed Cyg X-1 on 1996 June 14–25 (viewing period 522). The light curve of this observation is shown in Fig. 2. The flux is moderately variable, within a factor of ~2. The OSSE observation overlaps with six *RXTE* observations on June 17 and 18 (data sets 4–9). We have thus extracted six OSSE data sets (in the 50–1000 keV range) nearly simultaneous with the *RXTE* observations. However, in order to get better statistics, we have increased each OSSE data interval by 30 min on each side of the corresponding *RXTE* interval, as shown in Table 1. The OSSE data include energy-dependent systematic errors (estimated using both in-orbit and pre-launch calibration data), which range from ~3 per cent at 50 keV to ~0.3 per cent at ≳ 150 keV. We have also obtained the OSSE spectrum from the entire observation (data set 10). The excellent statistics of this spectrum allows a study of the average spectral properties in soft γ-rays, e.g., possible presence of an annihilation feature or a high-energy cut-off.

ASCA observed Cyg X-1 from 1996 May 30 5^h30^m to May 31 3^h20^m UT (Dotani et al. 1997). The GIS observation was made in the standard PH mode. The SIS data suffer from heavy photon pile-up and thus are not usable. The *ASCA* and *RXTE* observations on May 30 overlap only on a short period of time. Therefore, in order to improve the statistics, we used some *ASCA* data before and after the *RXTE* observation of the data set 3, which results in 1488 s of the net exposure time (which corresponds to about 4000 s of on-source data). Although the resulting *ASCA*/*RXTE* data are not strictly simultaneous, the constancy of the *ASCA* light-curve, shown in Fig. 3, strongly suggests constancy of the *ASCA* spectrum. We used the GIS response matrix v4.0.

Near-simultaneous *ASCA*/*RXTE* observations of this bright source provide us with an opportunity to study the cross-calibration of the instruments. Since the response matrices of X-ray detectors are not diagonal, we cannot compare detector counts directly. We can only choose a model spectrum, fit it to the data, and then compare the resulting spectra. For this, we use our best model (consisting of a disc blackbody and a non-thermal component) found in Section 3.5 below. We first fit the 0.7–10 keV *ASCA* data simultaneously with the 2–50 keV PCA and, in order to establish more firmly the high-energy continuum, with the 15–200 keV HEXTE data. Fig. 4(a) shows the data-to-model ratio for the best fit. We see that there are strong positive residuals at the high- and low-energy ends of the GIS and PCA spectra, respectively, indicating that the PCA spectrum is softer than the GIS one in the range of the overlap. In particular, in the lowest energy range of ~2.2–2.6 keV, the PCA channel flux exceeds the corresponding GIS flux by around 30 per cent, which corresponds to about 12σ. This discrepancy is probably due to uncertainties in the PCA response matrix, especially at the lowest energies. A better agreement between the GIS and PCA data can be obtained if only the PCA channels at ≥4 keV are used, as shown in Fig. 4(b). Then the PCA-to-GIS flux ratios at 4–4.3 and 9–10 keV become 0.96 and 1.08, respectively, and we use the 4–50 keV PCA data hereafter. The above uncertainty in determining the observed X-ray spectrum will then result in some systematic uncertainty in the parameters of our theoretical models.

After completion of the data fits presented in this paper, an updated version of the PCA response matrices was released as a

part of ftools v4.2 on 1998 December 10. We have then repeated the joint *ASCA*/PCA fit above with the new PCA response matrix, and found that the discrepancies reported above have remained virtually unchanged.

3 RESULTS

3.1 Models of absorption, disc emission and reflection

For spectral fits, we use xspec v10 (Arnaud 1996). The confidence range of each model parameter is given for a 90 per cent confidence interval, i.e., $\Delta\chi^2 = 2.7$ (e.g. Press et al. 1992). The spectra are absorbed by the interstellar medium with a column density N_H, for which we use the opacities of Morrison & McCammon (1983) and the abundances of Anders & Ebihara (1982). Since only the *ASCA* data constrain N_H (see Table 2 below), we assume $N_H = 5 \times 10^{21}$ cm^{-2} in all fits not including the *ASCA* data.

We fit the observed spectra by a sum of two main primary continua. The first one is due to blackbody emission of an accretion disc. We model it using the pseudo-Newtonian (hereafter PN) potential and taking into account the torque-free inner boundary condition; see Appendix A. The disc extends from an inner radius, R_{in}, corresponding to $r_{in} \equiv R_{in}/R_g$ (where $R_g \equiv GM/c^2$) to infinity, and its temperature distribution is parametrized by the maximum temperature, T_{max} reached by the disc. We assume $r_{in} = 6$ (i.e., at the minimum stable orbit in the Schwarzschild metric) unless stated otherwise. We assume $D = 2$ kpc and, in most fits, the disc inclination of $i = 45°$ (which is around the middle of the allowed range of i; see Section 1) and the colour-to-effective temperature ratio, $f_{col} \equiv T_{col}/T_{eff} = 1.7$ (Shimura & Takahara 1995).

The second primary continuum corresponds to the excess emission observed above the high-energy part of the disc emission. For that continuum, we use models described in Sections 3.2–3.4. This continuum is emitted outside the disc, and thus it is Compton-reflected from the disc surface.

For modelling Compton reflection, we use viewing-angle-dependent Green's functions of Magdziarz & Zdziarski (1995), which assume an isotropic point source (or, equivalently, an optically thin corona) above a slab. However, we treat $\Omega/2\pi$ as a free parameter, where Ω is an effective (i.e., corresponding to the observed strength of reflection) solid angle subtended by the reflector. The reflection is accompanied by an Fe fluorescence Kα line centred at an energy, E_{line}. When the reflection comes from a fast rotating disc in a strong gravitational potential, Doppler and gravitational shifts become important. We approximate these effects by convolving *both* the reflected component and the Fe Kα line with the Schwarzschild disc line profile of Fabian et al. (1989). For simplicity, the emissivity of the reflection and of the line as a function of a disc radius is assumed to vary as r^{-s}. We expect $s \sim 0$, 2 and 3 from different parts of the disc, depending on the geometry (see Fabian et al. 1989). We assume $s = 2$ unless stated otherwise. In calculating the relativistic distortion, we consider a range of radii from r_{in}, which equals that used for the disc blackbody emission, to $r_{out} = 1000$.

The reflected medium is photoionized, and the ionization is described by a parameter ξ. To allow direct comparison with other results, we follow Done et al. (1992) in the definition of the ionization parameter as $\xi \equiv 4\pi F_{ion}/n$, where F_{ion} is the 5 eV– 20 keV irradiating flux in a power-law spectrum, and n is the density of the reflector. (We note that in the soft state of Cyg X-1,

most of the ionizing photons have energies $\gtrsim 1$ keV, and a power-law shape of the irradiating continuum is only a rough approximation.) For simplicity, we assume that ξ is uniform in the medium. Since the ionization state of the disc close to the black hole will vary significantly with radius, the value of ξ found from the fits corresponds to an average ionization of matter at a range of radii from which most of reflection originates. The abundances in the reflector are those of Anders & Ebihara (1982), except the relative Fe abundance, A_{Fe}, which is allowed to be free in some models. The ion edge energies and opacities are from Reilman & Manson (1979), except that now the Fe K-edge energies are taken from Kaastra & Mewe (1993).

In our fits, we allow for free relative normalization of data from different instruments, except for the simultaneous PCA/OSSE data. In that case, we found that their relative normalization is fully consistent with unity.

3.2 Phenomenological description

As illustrated in Fig. 1, the Xγ spectrum of Cyg X-1 in the soft state consists of a blackbody-like soft component dominant below ~ 2 keV and a power-law tail extending to at least several hundred keV. In order to allow a comparison with previous results (Dotani et al. 1997; Zhang et al. 1997b), as well as to establish a phenomenological description of the spectral data, we start our analysis with a simple model consisting of a PN disc and a power law with its corresponding Compton-reflection continuum and an Fe line computed taking into account the relativistic smearing. First, we fit the simultaneous *RXTE*/OSSE data of June 17 and 18 (data sets 4–9). The photon spectral index, Γ, varies between about 2.3 and 2.5, which confirms the results of simultaneous ASM and BATSE monitoring of Cyg X-1 (Zhang et al. 1997b). The reflector solid angle, $\Omega/2\pi$, is ~ 0.6–0.7, and $\chi^2_\nu \sim 500/475$.
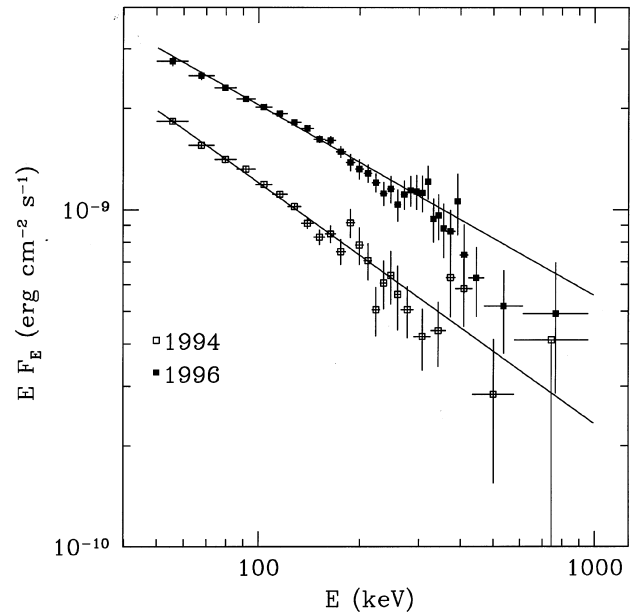

Figure 5. OSSE spectra of Cyg X-1 in the soft state of 1994 February (open boxes) and 1996 June (filled boxes). The former data come from the OSSE viewing period 318, 1994 February 1–8 (Phlips et al. 1996). The latter data are described in Table 1, observation 10. The two data sets are fitted by power laws with $\Gamma = 2.72^{+0.03}_{-0.04}$ and $2.57^{+0.02}_{-0.03}$, respectively (solid lines).

Next, we test the *RXTE*/OSSE data for a presence of a high-energy cut-off. We multiply the power law by an exponential factor with an e-folding energy, E_f. Since the simultaneous *RXTE*/OSSE observations constrain E_f only weakly, we test the properties of the high-energy tail using the OSSE data integrated over the whole viewing period 522 (data set 10), which spectrum is detected up to $\sim 800\,$keV (Fig. 5). When we fit together the *RXTE* data No. 5 and the integrated OSSE spectrum, the best-fitting e-folding energy is very high, $E_f = 940^{+800}_{-310}\,$keV.

On the other hand, a power-law hard continuum fails to reproduce the low-energy spectrum of the simultaneous *ASCA*/*RXTE* observation, which was pointed out by Gierliński et al. (1997b) and C98. A fit of a model consisting of a blackbody disc, a power law and the corresponding reflection continuum with an Fe Kα line provides a very poor fit to this data set, with $\chi^2_\nu \sim 1100/576$. A much better fit, with $\chi^2_\nu = 608/574$, can be obtained with a broken power-law continuum instead of a single power law. We find the power-law indices, $\Gamma_1 = 2.67^{+0.02}_{-0.03}$, $\Gamma_2 = 2.19 \pm 0.02$, the break energy, $E_{break} = 10.9 \pm 0.5\,$keV, $\Omega/2\pi = 0.48^{+0.09}_{-0.08}$, $N_H = (5.8 \pm 0.1) \times 10^{21}\,$cm^{-2}, $kT_{max} = 372^{+5}_{-7}\,$eV, $M_X = 9.4^{+0.4}_{-0.2}\,M_\odot$, $\xi = 2000 \pm 600\,$erg cm s^{-1}, $E_{line} = 6.38^{+0.16}_{-0.15}\,$keV, and the line equivalent width, EW $\approx 110\,$eV. These results are relatively similar to those of Dotani et al. (1997) and C98.

Furthermore, we stress that if the tail beyond the disc blackbody is due to Comptonization of the disc blackbody photons (as it is most likely the case in Cyg X-1), the tail spectrum would have a sharp low-energy cut-off at $\lesssim 2\,$keV. A proper description of the tail is then essential for determining the disc parameters. Using a continuum without an intrinsic low-energy cut-off (e.g., a power law) can result in an erroneous determination of the disc properties and N_H.

3.3 Thermal plasma model

As shown in the previous section, the high-energy power law in the soft state extends to very high energies ($E_f \gtrsim 600\,$keV). This contrasts the hard state, where the power law is cut off above $\sim 100\,$keV. If this spectrum were emitted by Comptonization of soft photons in a thermal plasma, the electrons would have to have a temperature of at least several hundred keV. Then, in order to account for the observed power-law slope, the optical depth of the electrons would have to be very low, $\lesssim 0.01$. Subsequent scattering events in a plasma with such very low optical depth would form distinct humps in the emerging spectrum, which are clearly not seen in the data. We confirm this using a thermal-Comptonization model of Coppi (1992), assuming that seed photons for Compton up-scattering are those emitted by the disc. This model (together with a disc, reflection and a line) fitted to the *RXTE*/OSSE spectra (data sets 4–9) yields unacceptable values of $\chi^2_\nu \sim 1000/476$, much worse than that obtained in Section 3.2 with a power-law incident continuum.

Furthermore, we find that the thermal-Comptonization model provides a very poor fit to the *ASCA/RXTE* data, as it is unable to reproduce the broken power-law shape of the tail. This result agrees with that of Cui et al. (1998, hereafter C98), who could fit those data with thermal Comptonization only, assuming that the temperature of seed photons is much higher than that of the observed disc photons. Thus we rule out the thermal Comptonization as a model for the continuum emission in the soft state of Cyg X-1.

3.4 Hybrid thermal/non-thermal plasma model

Since the high-energy tail in the spectrum cannot be due to emission from a thermal plasma, we fit the data using a non-thermal model of Coppi (1992) with some modifications (see also Coppi & Blandford 1990, Zdziarski, Coppi & Lamb 1990, Zdziarski, Lightman & Maciołek-Niedźwiecki 1993 and a recent review by Coppi 1999). This model embodies Compton scattering, $e^\pm$ pair production and annihilation, $pe^\pm$ and $e^\pm e^\pm$ thermal and non-thermal bremsstrahlung, and energy exchange between thermal and non-thermal parts of the $e^\pm$ distribution via Coulomb scattering. The seed photons for Compton scattering are those emitted by the PN disc. Selected e^- are accelerated to suprathermal energies, and the thermal part of the $e^\pm$ distribution can be additionally heated (apart from Compton heating/cooling and Coulomb heating by the non-thermal $e^\pm$). (A similar, thermal/non-thermal, model was used, e.g., by Holman & Benka 1992 for solar flares.)

This model assumes a spherical plasma cloud with isotropic and homogeneous distributions of photons and $e^\pm$, and soft seed photons produced uniformly within the plasma (Coppi 1992). The properties of the plasma depend on its compactness, $\ell \equiv \mathcal{L}\,\sigma_T/(\mathcal{R}\,m_e c^3)$, where $\mathcal{L}$ is a power of the source, $\mathcal{R}$ is the radius of the sphere, and σ_T is the Thomson cross-section. We specifically use a hard compactness, ℓ_h, which corresponds to the power supplied to the electrons, and a soft compactness, ℓ_s, corresponding to the power supplied in the form of soft seed photons. We assume $\mathcal{R} = 10^8\,$cm, but this value is important only for bremsstrahlung emission (which is negligible in our case), and for the Coulomb logarithm (see Section 4.2 below).

This spherical model is certainly an idealization of the hot plasma source in Cyg X-1, and we need to relate the model parameters to those corresponding to the actual Xγ source in Cyg X-1. Based on the strength of the blackbody and reflection components (Section 3.2), our preferred geometry is that of a hot corona above the surface of an accretion disc. Similar to a method of Björnsson & Svensson (1991), we consider a local spherical volume with a radius $\mathcal{R} = H/2$ inside the corona, where H is the
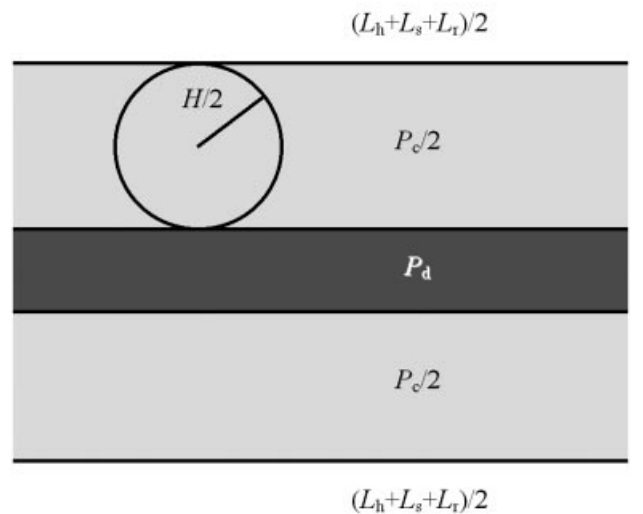

Figure 6. A sketch of the disc-corona geometry. The emission of the spherical plasma model is identified with that of the spherical region shown here. Power dissipated in the disc and corona is P_d and P_c, respectively. L_s, L_h, L_r are soft, hard and reflected luminosities, respectively. See Section 3.4 and Appendix B.

corona scaleheight, as shown in Fig. 6. In some models, we will also allow the corona to cover the disc at $R \lesssim R_h$ partially with the covering fraction, g (≤ 1).

We then consider the relation of the compactnesses, ℓ_h and ℓ_s, obtained from fitting the spherical model, to the parameters of the corona: the luminosity in scattered photons, L_h, the luminosity in unscattered blackbody photons, L_s, the characteristic radius of the corona, R_h, and H. This will allow us to constrain the last two quantities by the observed fluxes and fits of the model. For that purpose only, we assume that the corona radiates isotropically and neglect corrections due to the finite Thomson optical depth of the corona, the finite disc albedo, a, and the viewing angle of $i \neq 60°$ (in which case the anisotropy of the blackbody flux emitted by the disc plays a role). However, we do take into account those corrections later in considering the energy balance between the disc and the corona (Section 3.9 and Appendix B).

We point out here one significant difference between the spherical and disc-corona geometries. Namely, the sphere radiates away *all* of the power supplied to the electrons as well as that supplied as seed photons. On the other hand, the isotropic corona luminosity, L_h, corresponds to only *half* of the total coronal power, $2L_h$ (while the other half is radiated towards the disc and absorbed), whereas the disc luminosity, L_s, corresponds to all of the power in soft photons emitted by the disc. In our model fitting, we fit observed fluxes in soft and hard photons. Therefore we have to define ℓ_h in terms of the hard power radiated away (rather than the dissipated) by electrons in the spherical volume. This yields

$$\ell_h \approx \frac{1}{6g} \frac{L_h \sigma_T}{R_h m_e c^3} \frac{H}{R_h}.$$

(3)

We note that the numerical factor in this equation is not precise due to the approximations described above, which will introduce some systematic uncertainty in our determination of plasma parameters.

In models in this section, we assume $g = 1$, which corresponds to all the blackbody photons passing through the plasma. Then the soft compactness, ℓ_s, is to be defined in the same manner as in equation (3), except that L_h is replaced by L_s. If $g < 1$, we will distinguish between the soft compactness in photons incident on the hot plasma and that in soft photons freely escaping (Section 3.9).

The compactnesses corresponding to the electron acceleration and to the additional heating of the thermal part of the $e^{\pm}$ distribution are denoted as ℓ_{nth} and ℓ_{th}, respectively, and $\ell_h = \ell_{nth} + \ell_{th}$. In our fits, we use the ratio of ℓ_{nth}/ℓ_h as a parameter. The rate at which non-thermal electrons appear in the source is assumed to be a power law, $\dot{N}_{inj}(\gamma) \propto \gamma^{-\Gamma_{inj}}$, between the Lorentz factors of γ_{min} and γ_{max}. We hereafter assume $\gamma_{min} = 1.3$ and $\gamma_{max} = 1000$. A different choice of γ_{max} has a negligible effect on our results as long as $\gamma_{max} \gg \gamma_{min}$, since most of the power in the case of $\Gamma_{inj} > 2$ (see Table 2) is injected around γ_{min}. The effect of the choice of γ_{min} on our results is discussed in Section 4.2.

The injected electrons and pairs produced in photon–photon collisions lose energy by inverse-Compton scattering (at a rate of $\dot{\gamma}_{Compton} \propto \gamma^2$), so the equilibrium $e^{\pm}$ distribution is *softer* then that of injected electrons. This can be seen from the steady-state continuity equation,

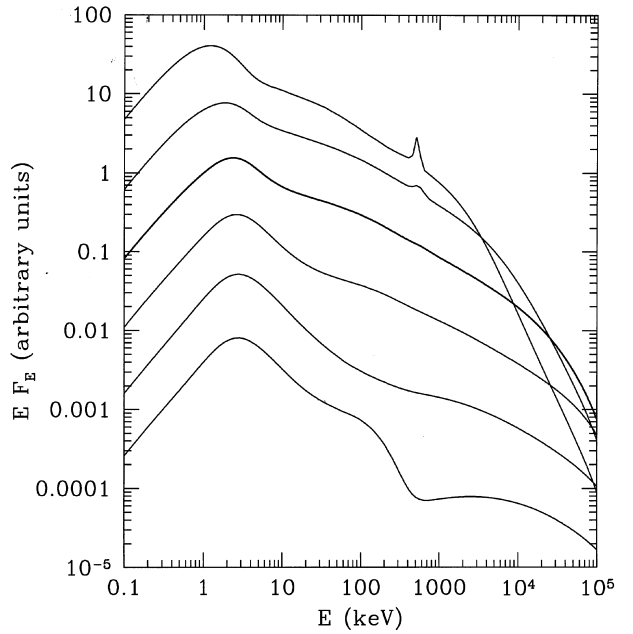$$\frac{d}{d\gamma}[\dot{\gamma} N_e(\gamma)] = \dot{N}_{inj}(\gamma),$$

(4)

Figure 7. Model spectra from non-thermal plasmas above the surface of an accretion disc calculated for varying soft compactness, ℓ_s. From bottom to top, $\ell_s = 0.01, 0.1, 1, 10, 100$ and 1000. Other parameters are $\ell_h/\ell_s = 0.3$, $\ell_{nth}/\ell_h = 0.9$, $\tau_i = 0.3$, $\Gamma_{inj} = 3$, $\gamma_{min} = 1.3$ and $kT_{max} = 0.4$ keV. At low and high compactness, we see distortions of the hard spectrum due to Coulomb interactions (see Section 4.2) and e^+e^- pair production and annihilation (see Section 3.6), respectively. Compton reflection and seed photons escaping from the plasma without a scattering are not included in the spectra shown. The normalization of each spectrum is arbitrary.

which solution leads to the non-thermal component of $e^{\pm}$ distribution, $N_e(\gamma) \propto \gamma^{-(\Gamma_{inj}+1)}$. Therefore the single scattering of seed photons off these $e^{\pm}$ forms a power-law spectrum with photon index $\Gamma \approx \Gamma_{inj}/2 + 1$. In steady state, the non-thermal and thermal $e^{\pm}$ have optical depths, τ_{nth} (typically $\ll 1$) and τ_{th}, respectively, following from balance of acceleration, pair production, and energy losses. The total optical depth is denoted by τ.

The optical depth of the thermal component, τ_{th} (typically $\gg \tau_{nth}$), is a sum of the optical depth to scattering on e^+e^- pairs and on e^- coming from ionization of atoms, τ_i. The latter is a free parameter of the model, but τ_{th} as well as the equilibrium temperature of the thermal component, T_e, are computed self-consistently.

The spectrum of the model is then used to compute the corresponding continuum from Compton reflection including relativistic smearing (Section 3.1). We find that the plasma in the source is so energetic that a single Compton scattering effectively removes a Compton-reflected photon from the reflection spectrum. Then, $\Omega/2\pi$ obtained from the fit corresponds to the unscattered part of Compton reflection.

A sequence of model spectra for varying compactness is presented on Fig. 7. For parameters consistent with the observations (as found in Section 3.5 below) the spectrum is basically a power law without a break up to $\sim 10^4$ keV. The power law is formed by a single inverse-Compton scattering of disc seed photons off the non-thermal $e^{\pm}$ with optical thickness of $\tau_{nth} \sim 10^{-2}$. At low energies, we see the spectrum of disc photons repeatedly scattered off the thermal $e^{\pm}$, as well as singly scattered off the non-thermal $e^{\pm}$. The former scattering dominates, forming a tail beyond the disc blackbody energies, crossing the non-thermal power law at ~ 10 keV.
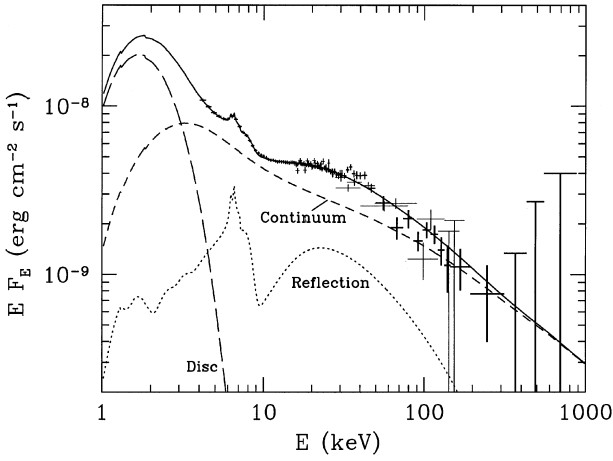
Figure 8. The simultaneous *RXTE* and OSSE observation of Cyg X-1 in the soft state on 1996 June 17 (observation No. 5) together with a model with $\tau_i = 0.25$ (solid curve; fit parameters given in Table 2). The model is decomposed into the hot-plasma emission (short dashes), Compton reflection including the Fe Kα line (dots), and the disc blackbody emission (long dashes).

3.5 Spectral fits with the hybrid model

In fitting the data, we have found we cannot uniquely determine the overall level of the compactness, which, in our fits, is given by the value of ℓ_s. The joint constraints from both the *ASCA/RXTE* and *RXTE/OSSE* data yield $5 \lesssim \ell_s \lesssim 20$. Since the ratio $\ell_h/\ell_s = 0.36^{+0.01}_{-0.02}$ is well established (see below), this corresponds to constraints on the hard compactness, $2 \lesssim \ell_h \lesssim 7$. The upper limit is due to the onset of efficient e^+e^- pair production at $\ell_h \gtrsim 7$ (see Fig. 7), whereas the data do not show any signatures of the presence of pairs (see Section 3.6). The lower limit is due to Coulomb cooling of non-thermal electrons becoming important at low compactness (see Fig. 7). At small ℓ_h this process thermalizes efficiently the non-thermal electrons below some Lorentz factor (see Section 4.2), whereas the data are consistent with a non-thermal distribution close to a power law. We hereafter assume $\ell_s = 10$ in most of fits below, and use ℓ_h/ℓ_s rather than ℓ_h as a free parameter.

We start spectral fitting with the June 17–18 *RXTE/OSSE* data (observations 4–9). We find that the data do not allow us to determine τ_i. There are several shallow local minima of χ^2 in a wide range of τ_i between ~ 0.2 and ~ 3. However, models with different values of τ_i differ significantly from each other below 4 keV, where we have no data. We find a strong correlation between τ_i and ℓ_h/ℓ_s, which latter parameter is also poorly determined by the data. Therefore, in order to determine τ_i and ℓ_h/ℓ_s, we use the *ASCA/RXTE* observation, for which we obtain $\tau_i = 0.25^{+0.05}_{-0.04}$ and $\ell_h/\ell_s = 0.36^{+0.01}_{-0.02}$ (see below). Since the spectral properties did not change significantly between 1996 May 30 and June 17–18, we assume that τ_i also remained similar, and we fix $\tau_i = 0.25$ in subsequent fits to the data sets 4–9. Fig. 8 shows the data set 5 fitted with $\tau_i = 0.25$. We further note that a large value of τ_i, say 2.5, would be difficult to reconcile within the coronal model, which we find below to be the most likely, with the presence of strong Compton reflection in the spectrum.

For the data sets 4–9, we find the best-fitting values of $\ell_{nth}/\ell_h \sim 0.95$–1 and corresponding 90 per cent confidence intervals covering the range of ~ 0.8–1. Thus, in order not to introduce unnecessary free parameters, we assume $\ell_{nth}/\ell_h = 1$ in our fits to the *RXTE/OSSE* data (see Table 2).

Subsequently, we study the *ASCA/RXTE* data of May 30. The 0.7–10 keV energy range of the GIS data allows us to determine the N_H, and therefore we let it be free in this fit. The low-energy coverage also allows us to better constrain the direct heating of thermal electrons, and thus we let ℓ_{nth}/ℓ_h be free. The fit results are shown in Table 2. The best-fitting parameters correspond to $\tau_{th} \approx 0.26$, $kT_e \approx 46$ keV, and $\tau_{nth} \sim 10^{-2}$. We now find the relative non-thermal power $\ell_{nth}/\ell_h = 0.77^{+0.05}_{-0.04}$, which, though somewhat less than unity, still confirms our conclusion that the direct thermal heating in Cyg X-1 in the soft state is weak compared to non-thermal acceleration. The above range of ℓ_{nth}/ℓ_h is still consistent with the results of June 17–18 *RXTE/OSSE* fits within the error bars, and thus we are not able to conclude whether the relative fraction of non-thermal power changed between May 30 and June 17–18 or not. The range of ℓ_s found above corresponds, at the fitted $\ell_h/\ell_s = 0.36^{+0.01}_{-0.02}$, to the total compactness, $\ell = \ell_s + \ell_h$, of $7 \lesssim \ell \lesssim 27$.

We note here that the actual value of ℓ_{nth}/ℓ_h depends somewhat on the assumed value of ℓ_s. This effect can be understood based on results of Section 4.2 below. Namely, the importance of Coulomb heating of the thermal $e^\pm$ plasma component by non-thermal electrons decreases with increasing compactness. Thus, more direct heating of the thermal $e^\pm$ is required at a higher compactness than at a lower one. Indeed, for the lower and upper limit of ℓ_s allowable by the data, 5 and 20, we find $\ell_{nth}/\ell_h = 0.88^{+0.08}_{-0.05}$ and $0.72^{+0.03}_{-0.02}$, respectively.

On 1996 May 22–23 (data sets 1 and 2), Cyg X-1 was in an intermediate state. The hard X-ray flux was significantly stronger than in soft-state observations of May 30 and June 17–18, but weaker than in the hard state (see Fig. 1). Although Cyg X-1 was observed during this period only by *RXTE*, we find that the shape of the spectrum allows a determination of τ_i. Fit results are given in Table 2. Since the soft component is relatively weak, we can only constrain the seed photon temperature, kT_{max}, to be $\lesssim 0.4$ keV, and we thus assume $kT_{max} = 0.3$ keV. We caution here that kT_{max} is strongly anticorrelated with R_{in}. For example, the data set 1 at $kT_{max} = 0.15$ keV yields R_{in} about 6 times larger than that for $kT_{max} = 0.3$ keV. We also obtain the compactness ratio of $\ell_h/\ell_s \sim 1$, which indeed places these data between the hard and soft states, for which $\ell_h/\ell_s \sim 10$ and 0.3–0.4, respectively.

Summarizing our results so far, we have found a satisfactory physical description of the data by a model with the main component due to Compton scattering of soft photons from an optically thick accretion disc in an optically thin, hot, plasma. We find that the plasma cannot be purely thermal. Rather, the electrons in the plasma have a hybrid distribution with a Maxwellian component at $kT_e \sim 40$–50 keV and a quasi-power-law, non-thermal, tail.

3.6 e^+e^- pairs

The optical depth of the thermal part of the $e^\pm$ distribution, τ_{th}, includes contributions from both ionization electrons ($= \tau_i$) and e^+e^- pairs. We find first that the *ASCA/RXTE* observation (data set 3) cannot constrain the presence of pairs. Fits with $\ell_s = 40$ and 10 with a χ^2 difference of only 2.2 yield $\tau_{th}/\tau_i \gg 1$ (a pair-dominated plasma) and 1.07 (an e^- dominated plasma), respectively. This is because a presence of pairs manifests itself primarily by an annihilation feature around 511 keV (see Section 4.2), which energy range is not covered by *RXTE*.

On the other hand, the *RXTE/OSSE* observations (data sets 4–9) do not constrain τ_i, as discussed in Section 3.5 above, which again
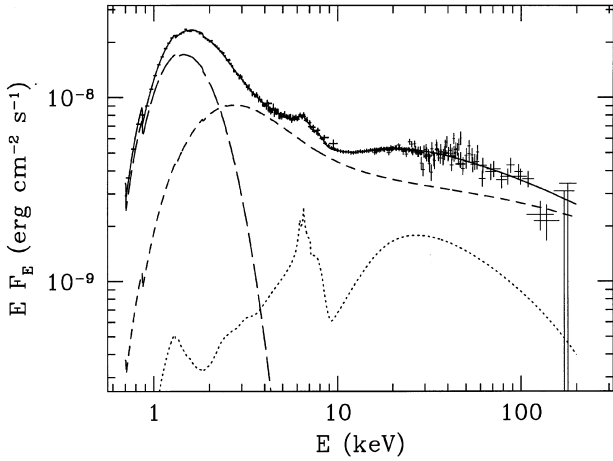
Figure 9. The simultaneous *ASCA* and *RXTE* observation of Cyg X-1 in the soft state on 1996 May 30 (observation No. 3). The short dashes, dots and long dashes show the Comptonization continuum, the component reflected from the cold disc, and the disc emission, respectively. The solid curve shows the sum. The fit parameters are given in Table 2. The Comptonization continuum is dominated by thermal and non-thermal scattering below and above, respectively, ~15 keV, with the resulting spectral break at that energy.

prevents us from constraining τ_{th}/τ_i. Therefore we fit the *ASCA/RXTE* data set 3 together with the average OSSE spectrum (data set 10). The presence of pairs is now excluded at a high statistical significance. At $\ell_s = 10$, $\tau_{th}/\tau_i \approx 1$, and at $\ell_s = 40$, which yields $\tau_{th}/\tau_i \approx 1.4$, χ^2 becomes significantly worse, $\Delta\chi^2 = +16$ at 626 d.o.f. The plasma becomes pair-dominated, $\tau_{th}/\tau_i \gg 1$, at $\ell_s = 60$, but then $\Delta\chi^2 = +20$. The main contribution to the increasing χ^2 comes from the OSSE channels around $m_e c^2$ due to an annihilation feature produced by the model but not present in the data. Thus, pairs appear to be negligible.

In our plasma model, we have assumed so far that the accelerated (or injected) particles are electrons rather than e^+e^- pairs (and the acceleration rate is balanced by the rate at which electrons move from the non-thermal distribution to the thermal one). On the other hand, some physical mechanisms may give rise to production of non-thermal pairs rather than electrons, as well as mostly pairs would be accelerated out of the thermal distribution if that is already pair-dominated. To investigate that case, we have considered a plasma model with an injection of e^+e^- pairs. However, this model gives an extremely poor fit to the data, $\chi^2_\nu \sim 1000/626$. This is due to the luminosity from annihilation of the injected pairs, which equals

$$L_{annihilation} \approx \frac{\Gamma_{inj} - 2}{(\Gamma_{inj} - 1)\gamma_{min}} L_h. \qquad (5)$$

The annihilation luminosity is then large in our case, with $\Gamma_{inj} \sim 2.5$ (Table 2) and γ_{min} constrained to be ~1 (see Section 4.2 below), which is in strong disagreement with the OSSE data showing no pair annihilation feature. Summarizing, the presence of a substantial number e^+e^- pairs in the Xγ source of Cyg X-1 in the soft state is ruled out.

3.7 Compton reflection and Fe Kα line

We find manifest signatures of reprocessing by a cold medium – an Fe K edge with a Kα line and a broad excess over the continuum at ~10–100 keV – in all our data sets. The most

straightforward interpretation of those features is in terms of Compton reflection of the hot-plasma emission by an ionized, optically thick, accretion disc. The statistical significance of the presence of reflection is very high. Fits to the data sets 3–9 without reflection are much worse, $\chi^2_\nu \sim 2$, than those including reflection (see Table 2), and the main cause of the bad fit is the strong residuals around the Fe edge/line energies. The intermediate-state *RXTE* data sets, 1–2, are somewhat less sensitive to reflection. Still, fits without reflection are much worse ($\chi^2 = 654$ and 586 at 425 d.o.f.) than those in Table 2.

Below, we use the simultaneous *ASCA/RXTE* observation (data set 3), which allows the most detailed study of Compton reflection and the associated Kα fluorescence. This is due to a broad energy range, ~0.7–100 keV, together with good sensitivity near 7 keV. First, we confirm that the reflected continuum is accompanied by an iron Kα line, by means of the standard *F*-test (e.g. Mises 1964). We apply here our best model (see Table 2) with relativistic Compton reflection with a line (described in Section 3.1) and without it. Our null hypothesis is that a model with the line fits the data better than a model without it. A fit without the line yields $\chi^2_1 = 652$ with $\nu_1 = 576$ d.o.f., whereas a fit with the line yields $\chi^2_2 = 618$, $\nu_2 = 574$ d.o.f. The chance function, $F_m = (\Delta\chi^2/\Delta\nu)/(\chi^2_2/\nu_2)$ has a Snedecor's *F* distribution. The significance level, $P(F > F_m)$, is the probability of committing an error of first kind, i.e., rejecting the correct hypothesis. For the fits above, $F_m = 15.6$ and $P(F > F_m) = 2.5 \times 10^{-7}$, which represents a very high statistical significance that an Fe Kα line is indeed present in the data.

We then investigate the issue of the width of the line. For that purpose, we first compare the *ASCA/RXTE* data to a model with static reflection (i.e., ignoring the relativistic effects) and a narrow Gaussian line. This yields a fit worse by $\Delta\chi^2 = +9$ compared to the fit in Table 2. This means that indeed the data are much better described by the line and reflection being relativistically smeared than by static line and reflection. Still, the disc inner radius is only weakly constrained by relativistic smearing, to $r_{in} \lesssim 50$ (in which fit we assumed the inner radius of the blackbody disc emission to be constant). Also, the value of the power-law index of reflection emissivity (Section 3.1) is only weakly constrained to $s \sim 2.1^{+0.5}_{-0.7}$. In order to compare with results of C98, we also considered a broad Gaussian line in the static-reflection model, obtaining a rather large width of $\sigma_{Fe} = 1.18^{+0.26}_{-0.22}$ keV (somewhat more than the values given by C98). Since uncertainties in the *RXTE*/PCA response matrix are not yet fully understood, we have checked our results by ignoring PCA data below 10 keV, in which case the Fe line parameters were constrained by *ASCA* data only. The results for the line energy and width turn out to be very similar to those obtained from the overlapping *ASCA/RXTE* data. Thus our conclusion is that the Fe Kα line in the soft state of Cyg X-1 is broad.

The reflecting medium is ionized, with $\xi = 350^{+250}_{-120}$ erg cm s^{-1}. Although observations on May 22–23 (data sets 1–2) and June 17–18 (data sets 4–9) yield higher values of ξ (see Table 2), those values are relatively weakly constrained and most of the data are consistent with the *ASCA/RXTE* result within 90 per cent confidence. Note that this ionization, obtained with our physical incident continuum, is much weaker than that found with our phenomenological, broken-power-law, continuum in Section 3.2, which shows the sensitivity of the fitted ionization parameter to the shape of the continuum around 7 keV.

The ionization state found here corresponds to a distribution of Fe ions peaking at Fe XXIII$^{+1}_{-II}$, and with Fe XXIV–XXVI constituting
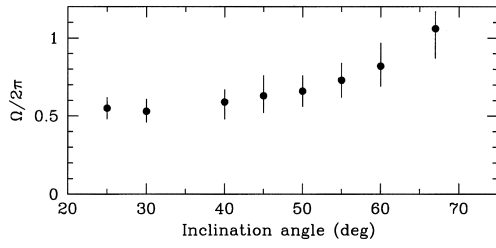
Figure 10. The dependence between the solid angle subtended by the reflector, $\Omega/2\pi$, and the assumed inclination angle, i. The error bars are given for 90 per cent confidence.

~30 per cent of the ion population. Due to resonant trapping followed by the Auger effect (e.g. Ross & Fabian 1993), Kα photons following ionization of Fe XVII–XXIII ions are completely destroyed and yield no contribution to the observed line. We thus would expect only a line from Fe XXIV–XXVI at ~6.7–7.0 keV. Instead, our model yields the rest frame centre energy of $E_{line} = 6.37 \pm 0.14$ keV for the *ASCA/RXTE* data, and ~6.3–6.5 keV for other *RXTE* observations. This inconsistency is likely to be due to our simplified model of reflection, with the ionization state uniform throughout the reflecting medium, whereas the ionization would, in general, vary considerably with the disc radius.

We also consider the Fe abundance, A_{Fe}, of the reflector. In all fits so far, we have assumed $A_{Fe} = 1$. We find that indeed $A_{Fe} = 1$ is consistent with the data. In particular, the *ASCA/RXTE* data fitted with A_{Fe} as a free parameter yield $A_{Fe} = 1.0^{+0.6}_{-0.4}$.

One parameter of Compton reflection which remains relatively uncertain is the inclination angle, i. As discussed in Section 1, the most conservative range of i is $25° \lesssim i \lesssim 67°$. The resulting $\Omega/2\pi \simeq 0.5$–1.0, increasing with the increasing i, is shown in Fig. 10. At the Doppler-tomography limit $i = 55°$ of Sowers et al. (1998), $\Omega/2\pi = 0.73 \pm 0.11$. Our fits favour large inclinations angles: $\chi^2 = 626$, 618 and 612 (for 574 d.o.f.) at $i = 25°$, 45° and 67°, respectively, similarly to a recent result of Done & Życki (1999) for the hard state of Cyg X-1. On the other hand, the plasma and disc properties, e.g., the values of ℓ_h/ℓ_s, ℓ_{nth}/ℓ_h, τ_i, T_{max}, are only weakly dependent on i.

3.8 Inclination and the black hole mass

If we assume that the disc extends to the minimum stable orbit in Schwarzschild metric, $r_{in} = 6$, the *ASCA/RXTE* data yield $M_X = 13.3^{+1.0}_{-0.8}$ M$_\odot$ at the assumed $D = 2$ kpc, $f_{col} = 1.7$ and $i = 45°$. We note that this mass range is *above* that allowed by equation (2) at $i = 45°$. However, as found in Section 3.7, the model parameters other than $\Omega/2\pi$ are insensitive to the assumed value of i. Thus M_X can be rescaled to other values of i using equation (A10), which yields

$$M_X = 11.2^{+0.8}_{-0.7} \frac{M_\odot}{\cos^{1/2} i}, \tag{6}$$

which holds for our data to an accuracy better than 2 per cent. This range of M_X overlaps with that of equation (2), provided that

$$0.13 \lesssim \frac{\sin^3 i}{(1 - \sin^2 i)^{1/4}} \lesssim 0.28, \tag{7}$$

which is satisfied for $29° \lesssim i \lesssim 39°$, corresponding (equation 6) to $14 \gtrsim M_X/M_\odot \gtrsim 11$. These are the mass and inclination ranges both consistent with fitting the X-ray data with a disc extending to

the minimum stable orbit and satisfying the constraints on the mass function and the mass ratio presented in Section 1.

However, this estimate neglects GR effects in the vicinity of a black hole, namely gravitational redshift and focusing. We can estimate these effects by introducing two factors, f_{GR} and g_{GR}, correcting the colour temperature and the integrated flux, respectively (Cunningham 1975; Zhang, Cui & Chen 1997a). Then the correction factor to the mass for a non-rotating black hole, $r_{in} = 6$, and $i \sim 35°$ to the mass is $g_{GR}^{-1/2} f_{GR}^2 \approx 0.83$ (with a slow dependence on i). Thus the above mass range becomes

$$M_X \approx (10 \pm 1) M_\odot, \tag{8}$$

which represents our best mass estimate including GR corrections. We note that this agrees very well with the estimates of Dotani et al. (1997) and C98 obtained using a GR disc model (after rescaling from $D = 2.5$ kpc used by them to 2 kpc).

This estimate is sensitive to uncertainties in the distance and the factor f_{col}, with $M_X \propto D f_{col}^2$. For example, a 20 per cent uncertainty in $D f_{col}^2$ would increase the range of i and M_X (after the GR correction) to $27° \lesssim i \lesssim 42°$, $14 \gtrsim M_X/M_\odot \gtrsim 7$.

Above, we assumed $r_{in} = 6$. However, the data do not require that. When we allow r_{in} to be a free parameter, the shape of the disc spectrum changes, and we find this change large enough to constrain r_{in} by the *ASCA/RXTE* data. Namely, the model fit to the data is improved by $\Delta\chi^2 = -6$ at $r_{in} = 17^{+26}_{-8}$. Other disc parameters are now $kT_{max} = 375^{+3}_{-5}$ eV and (at $i = 45°$ and before the GR correction) $M_X = 10^{+10}_{-7}$ M$_\odot$. In contrast to the $r_{in} = 6$ case, no additional constraints on the disc inclination can now be obtained from the X-ray data. However, our PN disc model does not take into account relativistic corrections to the shape of the observed disc-blackbody spectrum. Thus this result should be treated simply as a demonstration that the inner radius of a blackbody disc can, in principle, be constrained by X-ray spectral fits.

On the other hand, evolution of power spectra, X-ray time lags and the coherence function indicate that on 1996 May 30 (when the *ASCA/RXTE* observation fitted above was performed) the source was still in transition from the hard to the soft state, and the soft state was established only later, in particular during the *RXTE/OSSE* observations of 1996 June 17–18 (Cui et al. 1997). This would then support our finding of $r_{in} > 6$ during the *ASCA/RXTE* observation.

3.9 Energy balance

If the hot plasma (either homogeneous or patchy) forms a static corona above the disc, energy balance can be used to obtain the fraction of the gravitational energy released in the corona, f (Svensson & Zdziarski 1994, hereafter SZ94). The general solution to this problem is given by equation (B8) in Appendix B. We assume here isotropic emission of the corona (corresponding to $d = 1$ in that equation). The reflection albedo, a, is computed to be $a \simeq 0.25$ using our *ASCA/RXTE* model spectrum at $i = 65°$, at which the strength of Compton reflection is approximately equal to the reflection strength averaged over the 2π solid angle (Magdziarz & Zdziarski 1995). Since the plasma is optically thin, we assume the scattering probability, $p_{sc} \approx \tau_i \approx 0.25$. For the *ASCA/RXTE* model spectrum in the case of a homogeneous corona (see Section 3.4), we find the ratio of the hard flux, F_h (without including reflection), to the soft flux, F_s, to be $F_h/F_s \approx 0.50$. (The difference between this ratio and ℓ_h/ℓ_s is due to scattering of soft photons in the corona.) This corresponds to $L_h/L_s = 2(F_h/F_s)\cos i$ (see Appendix B). At

$i = 35°$ (see Section 3.8), $L_h/L_s \approx 0.82$. Equation (B8) then yields $f \approx 0.63$. Thus the geometry with a corona covering most of an inner disc is possible in the soft state.

On the other hand, the corona may be patchy (Haardt, Maraschi & Ghisellini 1994; Stern et al. 1995; Poutanen & Svensson 1996). We have investigated that possibility by adding an additional blackbody disc component to our model. The emission of that component corresponds to the fraction of the disc photons that are not passing through the corona. The remaining fraction, g', corresponding to the disc photons that are incident on the hot plasma, is $g' \gtrsim g$ (where g the covering fraction defined in Section 3.4), because the active regions of the patchy corona can be elevated above the disc surface. We have found that the addition of g' as a free parameter improves the fit by $\Delta\chi^2 = -9$, i.e., it is statistically significant. At the best fit, at which $g' = 0.55$, the flux ratio is $F_h/F_s = 0.53$. This then gives, from equation (B8), $f = 0.46$, relatively close to f in the homogeneous-corona case in the paragraph above.

3.10 Luminosity and accretion rate

The total luminosity in the soft state is, using the *ASCA/RXTE* spectrum (see Appendix B),

$$L = L_h + L_r + L_s = 4\pi D^2 \left[F_h(1 + a\Omega/2\pi) + \frac{F_s}{2\cos i} \right]. \quad (9)$$

The observed $F_h = 3.9 \times 10^{-8}\,\mathrm{erg\,cm^{-2}\,s^{-1}}$ and $F_s = 7.8 \times 10^{-8}\,\mathrm{erg\,cm^{-2}\,s^{-1}}$ yield, at $i = 35°$, $L \approx 4.5 \times 10^{37}\,\mathrm{erg\,s^{-1}}$. This corresponds to $\sim 0.03 L_E$ at $M_X = 10\,\mathrm{M_\odot}$. Here, $L_E \equiv 4\pi\mu_e GM_X cm_p/\sigma_T$ is the Eddington luminosity, where $\mu_e = 2/(1 + X)$ is the mean electron molecular weight, and $X \approx 0.7$ is the hydrogen mass fraction.

If we assume $r_{in} = 6$ and no advection, this corresponds to $\dot{m} \equiv \dot{M}c^2/L_E \approx 0.5$, or $\dot{M} \approx 8 \times 10^{17}\,\mathrm{g\,s^{-1}}$. On the other hand, $\dot{M}$ can be obtained from fitting the disc model at known M_X and L_s/L (see equation A7). As expected, this yields the same $\dot{M}$ as above.

4 DISCUSSION

4.1 Geometry and scaleheight of the corona

We consider here constraints on the geometry of the Xγ source from the plasma compactness. For the model spectrum for the *ASCA/RXTE* data, $L_h \approx 1.9 \times 10^{37}\,\mathrm{erg\,s^{-1}}$ (see above). The hard compactness is constrained to $2 \lesssim \ell_h \lesssim 7$, which follows from $5 \lesssim \ell_s \lesssim 20$ and $\ell_h/\ell_s \approx 0.36$ (Section 3.5). From equation (3), we find the characteristic radius of the hot corona is then $R_h \approx (H/gR_h)(1.2–4) \times 10^7\,\mathrm{cm}$. At the black hole mass of $10\,\mathrm{M_\odot}$ (see Section 3.8), this corresponds to $R_h \approx (8–30)(H/gR_h)R_g$.

We can determine H if we assume hydrostatic equilibrium of the corona. The pressure in the corona has contributions from radiation, thermal and non-thermal electrons and ions, and magnetic field. We find that if the ion temperature, T_i, equals T_e, the dominant contribution to pressure in the corona is from radiation. We then use equation (45) in SZ94 to estimate $H/R_h \sim 10^{-2}$ in the case of a homogeneous corona ($g = 1$) at the radius of maximum disc dissipation per log R, $17R_g$. This would imply a rather small size of the plasma, $R_h \lesssim 0.3g^{-1}R_g$, violating our assumption of a homogeneous corona, and thus implying $g \ll 1$. On the other hand, $T_i \gg T_e$ is a likely condition in many astrophysical situations, e.g., two-temperature coronae are considered by Di Matteo, Blackman & Fabian (1997). In addition,

ions can be accelerated to non-thermal energies, in addition to accelerated electrons. Then the corona may be supported by the ion pressure, together with the pressure of an equipartition magnetic field.

We can constrain the average energy of ions by requiring that the rate of Coulomb energy transfer from the ions (both thermal and non-thermal) to electrons corresponds a luminosity, $L_{Coulomb}^{ie} \ll L_h$, which follows from our fits, in which $\ell_{th} \ll \ell_h$. This, via the condition of hydrostatic equilibrium, constrains in turn the scaleheight of the corona. We then obtain, using equations (1) and (3) in Zdziarski (1998),

$$\frac{H}{R_h} \approx 2 \times 10^2 \Theta_e^{3/2} \tau_{th}^{-2} \frac{L_{Coulomb}^{ie}}{L_E} \approx \frac{L_{Coulomb}^{ie}}{L_h}, \quad (10)$$

where $\Theta_e \equiv kT_e/m_e c^2$; this holds independent of radius. In the second equality, we used the numerical values of the parameters corresponding to the plasma in Cyg X-1. Then, for example, $H/R_h = 0.3$ (corresponding to $\ell_{th}/\ell_h \sim 0.3$, see Section 3.5) would correspond to $R_h \approx (6–20)R_g$ at the covering fraction of $g \approx 0.5$ (Section 3.9). Thus the hot plasma can extend over a substantial part of the disc region where most of the gravitational energy is dissipated. We note that H/R_h of equation (10) corresponds subvirial ions, $kT_i/m_p c^2 \sim 0.05/r$.

On the other hand, the corona is not necessarily in hydrostatic equilibrium (e.g. Beloborodov 1999). Some of the power released in the corona can be used to accelerate it to some velocity, βc. We can constrain β by considering the power (or kinetic luminosity), L_{kin}, of the outflowing ions, which equals the number flux times the bulk-motion energy times area. This yields

$$\frac{L_{kin}}{L_h} \approx \frac{m_p}{m_e} \frac{\tau \beta^3}{2\ell_h}. \quad (11)$$

For $\tau \sim 0.25$ and $2 \lesssim \ell_h \lesssim 7$ (Section 3.5), $\beta \gtrsim 0.3(L_{kin}/L_h)^{1/3}$. Since no apparent effects of eventual dissipation of L_{kin} are observed from Cyg X-1, probably $L_{kin} \ll L_h$. Then equation (11) allows for a mildly relativistic outflow, e.g., $\beta \sim 0.2$ at $L_{kin} \approx 0.2L_h$ and $\ell_h = 7$.

4.2 Coulomb interactions and plasma heating

As found in Section 3.5, the *ASCA/RXTE* data require $7 \lesssim \ell \lesssim 27$. The upper limit is due to effects e^+e^- pair production and annihilation, and the lower limit is due to energy loss of non-thermal electrons by Coulomb scattering.

The origin of the lower limit has been discussed by Poutanen (1999; see also Zdziarski et al. 1990). For completeness, we discuss it in some detail here. The energy loss rate due to Compton scattering is (e.g. Rybicki & Lightman 1979)

$$\dot{\gamma}_{Compton} \approx -\frac{4}{3} \frac{\sigma_T}{m_e c} (\gamma^2 - 1) U_{ph}, \quad (12)$$

where U_{ph} is the energy density of photons for which Compton scattering is in the Thomson limit. For a homogeneous, optically thin, spherical source of radius $\mathcal{R}$ and with luminosity $\mathcal{L}$, the energy density is roughly

$$U_{ph} \approx \frac{\mathcal{L}}{(4/3)\pi\mathcal{R}^3} \frac{\mathcal{R}}{c} = \frac{3}{4\pi} \frac{m_e c^2}{\sigma_T} \frac{\ell}{\mathcal{R}}, \quad (13)$$

where we use $\ell \approx \ell_s + \ell_h$ for the soft state of Cyg X-1, in which most of photons in the observed spectrum are in the Thomson limit. On the other hand, the Coulomb energy loss rate due to

interaction of an electron of $\gamma \gg 1$ and $\gamma - 1 \gg \Theta_e$ with a background thermal plasma is given by (Gould 1975; Frankel, Hines & Dewar 1979; Coppi & Blandford 1992)

$$\dot{\gamma}_{\text{Coulomb}} \approx -\frac{3}{2}\frac{c}{\mathcal{R}}\tau_{\text{th}}\ln(\Lambda\gamma^{1/2}), \tag{14}$$

where $\Lambda = [2\mathcal{R}/(3a_0\tau_{\text{th}})]^{1/2}$, and $a_0 = 5.29 \times 10^{-9}$ cm is the Bohr radius. Then the two rates are equal at a critical Lorentz factor given by

$$\gamma_{\text{cr}}^2 \approx \frac{3\pi\tau_{\text{th}}}{2\ell}\ln\Lambda + 1. \tag{15}$$

Note that γ_{cr} depends on $\mathcal{R}$ only weakly via $\ln\Lambda$, and thus this result is nearly independent of the source geometry. Since $\dot{\gamma}_{\text{Coulomb}} \propto \gamma^0$ while $\dot{\gamma}_{\text{Compton}} \propto \gamma^2$, the Coulomb energy loss is so fast that it creates a break at γ_{cr} in the non-thermal distribution. This then results in a break in the distribution of scattered photons, which is *not* seen in our data. Also, the energy lost by the non-thermal electrons strongly heats the thermal plasma, increasing its temperature. These effects are especially pronounced for $\Gamma_{\text{inj}} > 2$ (as is the case in our models), when most of the non-thermal energy is provided to accelerated electrons at the low-energy end of their distribution.

Since $\gamma_{\text{crit}} \propto \ell^{-1/2}$, the observed lack of signatures of the above effect constrains ℓ from below. At the lower limit of $\ell \approx 7$, and at $\tau_{\text{th}} = 0.25$, $\mathcal{R} = 10^8$ cm, $\gamma_{\text{cr}} \approx 2$, i.e., Coulomb interactions just begin to affect the low-energy end of the non-thermal distribution. Fig. 7 illustrates the effect of varying compactness on the spectral shape.

In most of our fitted models, we found Coulomb heating of the thermal plasma sufficient to maintain the plasma temperature required by the observed spectral shape, $kT_e \sim 50$ keV (which, we note, is much higher than the Compton temperature, ~ 1 keV, at which the net energy transfer via Compton scattering between electrons and photons of the observed spectrum would be null). Thus $\ell_{\text{nth}}/\ell_h \approx 1$ in those models (Section 3.5). However, this result depends on γ_{min}, which has been set so far to 1.3. A higher value of γ_{min} would decrease the Coulomb heating and would require some additional heating of the thermal plasma component. For example, the *ASCA/RXTE* data fitted with $\gamma_{\text{min}} = 3$ yield $\ell_{\text{nth}}/\ell_h = 0.62$, i.e., additional heating is required. However, this fit is worse by $\Delta\chi^2 \approx +9$ with respect to the fit with $\gamma_{\text{min}} = 1.3$. Thus γ_{min} is constrained by the data to be ~ 1.

Some additional heating of the thermal electrons can be due to the Coulomb energy transfer from energetic ions (see Section 4.1). The ions can be thermal or non-thermal. Acceleration of ions is, in fact, quite likely, and not in conflict with the data. In Section 3.5 we found that the electron acceleration rate, $\dot{N}_{\text{inj}}$, is soft, with most of the accelerated electrons near $\gamma_{\text{min}} \sim 1$. If the acceleration of ions follows a similar law, most of the accelerated ions will have energies close to the low-energy end of the power law, and effects of pion and pair production by ions will be negligible. On the other hand, the accelerated ions will provide some contribution to Coulomb heating of the thermal electrons (and to the pressure in the plasma), which contribution is allowed by the data as long as the average ion energy is $\lesssim 50$ MeV$/r$ (see Section 4.1). We also note that the energetic ions would transfer some energy to the non-thermal electrons via Coulomb scattering. However, this rate, inversely proportional to the ion mass, is found by us to be negligible compared to the energy loss rate of non-thermal electrons to the thermal ones (equation 14).

Another mechanism of heating the thermal electrons is the so-called synchrotron boiler (Ghisellini, Guilbert & Svensson 1988;

Ghisellini, Haardt & Svensson 1998; Svensson 1999). In this process, thermal electrons are heated by synchrotron reabsorption of photons emitted by the non-thermal electrons.

4.3 Anisotropy effects

As stated in Section 3.4, our Comptonization model assumes all the distributions (photons and $e^\pm$) to be homogeneous and isotropic. This approximation may not hold in some geometries. In particular, in the disc-corona geometry, the seed photons enter the corona from below only. Thus their distribution is anisotropic. Then a soft photon emitted by the disc surface is much more likely to scatter on an energetic electron moving down rather than up. This is because the scattering probability is $\propto 1 - (v/c)\cos\vartheta$, where v is the electron speed, and ϑ is the angle between the directions of the electron and the photon. This anisotropy affects in different ways spectra from non-thermal and thermal plasmas (and their $e^\pm$ distributions), and thus we discuss them separately.

The case of a relativistic, non-thermal $e^\pm$ distribution is studied by Ghisellini et al. (1991). Their results show that the angle-averaged downward flux, due to a single Compton scattering by isotropic electrons with $\gamma \gg 1$, is ~ 3 times larger than the flux emitted upwards at the angle of $45°$. This would result in a corresponding strong enhancement of the Compton-reflected component, which effect is clearly not seen in our data. This enhancement could be much smaller if the hot plasma forms an inner hot disc and emission of seed photons and reflection are from an outer optically thick disc.

On the other hand, the steady-state non-thermal electron distribution in a disc corona is unlikely to be isotropic. This is because electrons directed downward lose energy much faster than those directed upward, due to precisely the same effect as that discussed above. The main mechanism for their isotropization is Coulomb interaction, since higher order Compton scatterings are negligible in our case with $\tau_{\text{nth}} \sim 10^{-2}$. The process of Coulomb interactions of non-thermal electrons with the background thermal plasma is considered in Section 4.2 above, where we found that the observed spectrum constrains compactness to a range where the electron energy losses due to this process are negligible compared to those due to Compton scattering. Then the negligible energy losses, in the case of $e^\pm e^\pm$ scattering, imply no significant changes of the direction of the relativistic electrons. (The rate of interactions of relativistic electrons with protons, which could change the electron direction without significant energy loss, is smaller than that with $e^\pm$ by a factor m_e/m_p and thus even less significant.) Thus the steady-state distribution of electrons with $\gamma > \gamma_{\text{cr}}$ ($\gtrsim 2$; equation 15) will be strongly anisotropic due to the Compton energy loss rate depending on the direction.

When this is the case, an isotropic acceleration/injection of relativistic electron will lead to *isotropic* emission of singly scattered photons. This is because the effects of anisotropic emission and anisotropic energy loss cancel each other, and the rate of emission in a given direction is simply proportional to the injection rate (see Ghisellini et al. 1991).

Note that an anisotropic electron distribution corresponds to a current in the plasma. This current will be balanced by an opposite current in the thermal component of the electron distribution. Since $\tau_{\text{th}} \gg \tau_{\text{nth}}$, the latter current will have a negligible effect on the properties of the thermal plasma component.

Anisotropy effects in the case of a thermal $e^\pm$ distribution are considered by Haardt (1993), Stern et al. (1995) and Poutanen &

Svensson (1996). They are due to the same physical effect as described above, and thus they suppress a part of the emitted spectrum due to the first (and, to some degree, second) order of Compton scattering. On the other hand, photons become closely isotropic after a higher number of scatterings. This leads to the so-called anisotropy break close to the peak energy of the second-order scattering. In contrast to the non-thermal case, we have found that the Coulomb relaxation time for the thermal electrons interacting with themselves is about equal to the thermal plasma cooling time ($\sim 10^{-4}$ s), and thus no significant anisotropy of the thermal electron distribution is expected in our case.

In order to assess the significance of the thermal anisotropy break in the case of Cyg X-1, we have performed Monte Carlo simulations for a slab geometry, assuming the plasma parameters as found from data fitting. We have found the anisotropy break at ~ 15 keV, with the outward flux at 7 keV suppressed by a factor of ~ 0.8 with respect to the isotropic case. As seen in Fig. 9 (the dashed curve), this break energy actually coincides with the break occurring due to intersections of the power laws due to thermal and non-thermal scattering. Then plasma parameters slightly different from those determined neglecting anisotropy effects could still produce the observed spectrum. Thus the present data are still consistent with the presence of a thermal anisotropy break.

On the other hand, if the mildly relativistic outflow is present in the corona (see Section 4.1), the seed soft radiation emitted by the disc is more isotropic in the rest frame of the outflowing plasma, thus reducing the amplitude of the anisotropy break (see Beloborodov 1998, 1999).

4.4 Disc stability

We examine here the stability of the optically thick disc, taking into account the fraction, f, of the gravitational energy being dissipated in the corona (SZ94). A possible mechanism for energy transfer from the disc to the corona is magnetic flares (e.g. Galeev, Rosner & Vaiana 1979; Beloborodov 1999). A part of the disc becomes radiation-pressure-dominated and thus unstable (both thermally and viscously) above a critical accretion rate, $\dot{m}_{cr}$. We find that a radiation-pressure-dominated zone in a PN disc appears
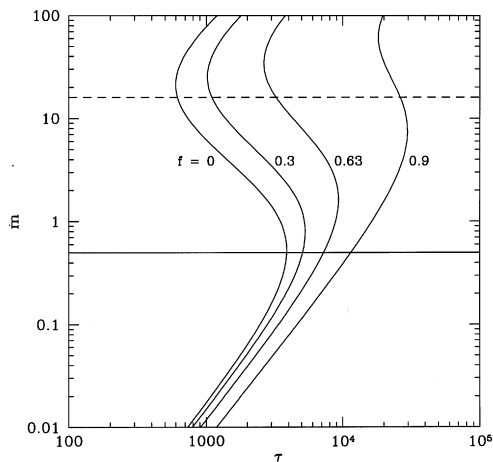

Figure 11. The solutions of the optically thick disc (Abramowicz et al. 1988) with a fraction of accretion power, f, dissipated in the corona (SZ94), for $M_X = 10 \, M_\odot$ and $\alpha = 0.1$ at the radius of the most significant instability of $R = 15.1 R_g$. The curves are labelled by their value of f, with $f = 0.63$ corresponding for Cyg X-1. The solid and dashed horizontal lines correspond to the accretion rate of Cyg X-1 in the soft state and to the Eddington luminosity at an efficiency of $\eta = 1/16$, respectively.

first (with increasing $\dot{m}$) around $R = 15.1 R_g$. We then extend results of SZ94 (who considered the Newtonian potential) to the case of the PN potential, and derive $\dot{m}_{cr}$ in the presence of external dissipation as

$$\dot{m}_{cr} = 0.64(\alpha M_X/M_\odot)^{-1/8}[(1-f)\zeta]^{-9/8}, \qquad (16)$$

where α is the viscosity parameter, and ζ is a parameter in the vertically averaged radiative transfer equation, which is set by various authors between 0.5 and 2. We follow here Shakura & Sunyaev (1973) and set $\zeta = 1$ (this value is in approximate agreement with calculations taking into account the vertical disc structure; A. Różańska, private communication). We note that relativistic effects, as approximated by the PN potential, have a stabilizing effect on the disc, i.e., they increase the value of $\dot{m}_{cr}$. Specifically, the numerical coefficient in equation (16) is only 0.37 in the Newtonian case (SZ94).

At $M_X = 10 \, M_\odot$, $f = 0.63$, $\dot{m}_{cr} \approx 1.47\alpha^{-1/8}$. This implies that the disc in the soft state of Cyg X-1, with $\dot{m} \approx 0.5$ (Section 3.10), is stable at any α. Fig. 11 shows the solutions of the optically thick accretion disc with the corona for four values of f.

On the other hand, the data do not require $r_{in} = 6$, and a fit in Section 3.8 gives $r_{in} = 17^{+26}_{-8}$. This solution corresponds to a higher $\dot{m}$ and a lower M_X than in the case of $r_{in} = 6$. Then $\dot{m}$ may possibly exceed $\dot{m}_{cr}$, and the disc instability may be responsible for the large r_{in}. The precise value of $\dot{m}$ in this case depends on the unknown partition of the observed luminosity into the fractions from the corona above the disc and an inner hot flow at $r < r_{in}$, possibly advective (Abramowicz et al. 1995; Narayan & Yi 1995). Therefore the current data do not allow us to distinguish between the possibilities of $r_{in} = 6$ and > 6.

4.5 Alternative models

One alternative model to the non-thermal Compton model presented here is thermal Comptonization, which was proposed to model spectra of the soft state of Cyg X-1 (Poutanen, Krolik & Ryde 1997; C98; Esin et al. 1998) and other black hole binaries (Miyamoto et al. 1991; Esin, McClintock & Narayan 1997). However, as discussed in Section 3.3, this process is unable to account for the observed steep power-law tails extending to high energies.

Another possibility for the production of the power-law spectra observed in the soft state is that of bulk-motion Comptonization (see, e.g., Payne & Blandford 1981, Colpi 1988 and Laurent & Titarchuk 1999). If there is quasi-spherical accretion near the black hole, then cold infalling electrons could acquire substantial velocities $v \sim c$, and Comptonization using the large bulk inflow velocity of the electrons (as opposed to their assumed smaller thermal motions) could give rise to power-law spectra like those observed in the soft state. This model predicts $\Gamma \simeq 3.8$ at $\dot{m} = 0.5$ (see Table 2 in Laurent & Titarchuk 1999) as well as a sharp cut-off in the spectrum at a few hundred keV. The OSSE data, on the other hand, clearly show $\Gamma \sim 2.6$ and no cut-off until at least 800 keV, which both strongly rule out the bulk-Comptonization hypothesis.

Also, only a fraction, $\ll 1$, of the disc blackbody photons (emitted semi-isotropically with maximum emission per $\log r$ at $r \sim 20$) will be incident on the inner spherical inflow (see figs 1 and 2 in Laurent & Titarchuk 1999). This appears to lead to a normalization of the tail spectrum with respect to the disc blackbody much below the observed normalization. Furthermore, the presence of the Compton reflection with a covering factor of

$\Omega/2\pi \sim 0.7$ puts strong constraints on the geometry of the accretion flow. Such a covering factor is natural in a disc-corona geometry, but it appears incompatible with the bulk Comptonization scenario (figs 1 and 2 in Laurent & Titarchuk 1999).

4.6   The nature of state transition

A remarkable feature of state transitions in Cyg X-1 is that the associated change in the bolometric luminosity is very small. We have found $L \approx 4.5 \times 10^{37}\,\mathrm{erg\,s^{-1}}$ in the soft state (Section 3.10), whereas the maximum bolometric luminosity observed in the hard state is $\sim 3 \times 10^{37}\,\mathrm{erg\,s^{-1}}$ (G97; at $D = 2\,\mathrm{kpc}$). If there is no advection, the corresponding change of $\dot{M}$ is small. In the simplest scenario, we expect no advection in the soft state, provided that the optically thick disc extends to the minimum stable orbit. On the other hand, a commonly used model for the hard state comprises a hot inner disc (Poutanen et al. 1997; Esin et al. 1998; Poutanen & Coppi 1998; Poutanen 1999), in which case advection is likely. If the transition from the hard state to the soft one is associated with an increase of $\dot{M}$, both that increase and the advected fraction of the power in the hard state have to be very small (Esin et al. 1998). On the other hand, advection may dominate over cooling in the hard state, in which case the hard-to-soft transition would be associated with a *decrease* of $\dot{M}$.

In either of the above cases, the hard-to-soft state transition appears to be associated with a decrease of the minimum radius of the optically thick disc, R_{in}. When R_{in} is large, the inner disc is hot and it receives a major fraction (~ 0.9) of the available gravitational energy. The spectrum is hard, $\Gamma \sim 1.6$, and the covering angle of the reflector is relatively small, $\Omega/2\pi \sim 0.3$. At a certain moment, the cold disc starts to move inwards, taking in more and more accretion power, while the hot phase diminishes. In the final configuration the cold disc extends down to near the last stable orbit, while the hot (non-thermal) plasma probably forms a corona above that disc, receiving less of the accretion power (~ 0.6) than in the hard state. This results in a softening of the spectrum, to $\Gamma \sim 2.5$, and an increase of the strength of the Compton-reflection component, to $\Omega/2\pi \sim 0.7$.

Another possible model for the hard state has recently been proposed by Beloborodov (1999). In that model, the Xγ source forms a corona above optically thick disc extending close to the minimum stable orbit even in the hard state. The hardness of the spectrum and the weakness of Compton reflection in that state are then explained by a mildly relativistic bulk motion away from the disc. The hard-to-soft state transition would then involve the corona becoming static. This may possibly be due to the coronal plasma consisting of e^+e^- pairs in the hard state (which is allowed by the form of hard-state spectrum; G97; Poutanen & Coppi 1998), and of an ordinary plasma in the soft state. The data studied here appear not to allow distinguishing between these possibilities.

5   CONCLUSIONS

In this work we have obtained a self-consistent description of the soft state of Cyg X-1 (observed in 1996 by *ASCA*, *RXTE* and OSSE) in terms of a (predominantly) non-thermal corona above the surface of an optically thick accretion disc. Emission of the non-thermal corona accounts for both the high-energy power-law tail observed up to several hundred keV and the soft excess, resolving two problems of the thermal-plasma model of C98.

The non-thermal corona receives most of the supplied power in the form of electrons accelerated (or injected) to relativistic energies. The acceleration rate is rather soft, with the power-law index of $\Gamma_{\mathrm{inj}} \sim 2.5$–3 above $\gamma_{\mathrm{min}} \sim 1$. The electrons lose their initial energy in Compton and Coulomb processes, and finally form a thermal component (at $kT_e \sim 50\,\mathrm{keV}$) of their distribution at low energies. The resulting Xγ spectrum consists of blackbody photons emitted by the disc (at low energies) and a component due to Compton up-scattering of the disc photons by both thermal and non-thermal electrons in the corona.

Production of e^+e^- pairs is negligible in the corona, which follows from the observed lack of an annihilation feature in the spectrum from OSSE. This constrains from above the compactness (a ratio of the luminosity to the size), ℓ, of the source. On the other hand, Coulomb scattering is an important process in heating the thermal electrons by the non-thermal ones. Still, the Coulomb energy loss by non-thermal electrons is constrained by the observed spectrum to be slower than their Compton energy loss, which constrains ℓ from below. The resulting constraints are $7 \lesssim \ell \lesssim 30$.

We also find that a modest heating of the thermal electrons (in addition to their Coulomb heating by the non-thermal electrons) is required by the observed spectrum. This heating can be provided by Coulomb interactions with energetic ions in the corona, which then also provide most of the pressure support of the corona.

The coronal geometry of the source is supported by the observed spectral component from Compton reflection from the disc surface and the Fe broad Kα fluorescence line. Both components are relativistically smeared, supporting reflection from an inner part of the disc. The strength of the observed Compton reflection spectrum is fully consistent with reflection from a slab, after taking into account Compton scattering of reflected photons in the coronal plasma. The observed softness of the spectrum is consistent with energy balance in the disc-corona system with $f \sim 0.6$ of the available gravitational energy dissipated in the corona (and the remainder within the disc). From the observed luminosity and fitted compactness, we find that the corona covers a substantial fraction of the disc, provided that most of its pressure support is provided from energetic ions. Still, the ion energy in random velocities is constrained to be much below the virial energy (by the constraint on the Coulomb heating of thermal electrons; see above). Then the corona can be static. On the other hand, we find that a mildly relativistic outflow is also consistent with the observations.

Fits of our PN disc model together with the mass function and constraints on the mass ratio imply $M_X \simeq (10 \pm 1)\,\mathrm{M_\odot}$ and the inclination of $i \sim 30°$–$40°$, at the most likely distance of $2\,\mathrm{kpc}$ and the colour correction of $f_{\mathrm{col}} = 1.7$. The bolometric luminosity is $\simeq 4.5 \times 10^{37}\,\mathrm{erg\,s^{-1}} \simeq 0.03 L_E$, which corresponds, in the absence of advection, to $\dot{m} \simeq 0.5$. At that accretion rate, the disc is fully stable all the way down to the minimum stable orbit against the instabilities associated with the dominance of radiation pressure. On the other hand, solutions with advection, a higher $\dot{m}$, and the disc terminating at $r_{\mathrm{in}} \gg 6$ are also allowed by the data.

REFERENCES

Abramowicz M. A., Czerny B., Lasota J. P., Szuszkiewicz E., 1988, ApJ, 332, 646

Abramowicz M. A., Chen X., Kato S., Lasota J. P., Regev O., 1995, ApJ, 438, L37

Anders E., Ebihara M., 1982, Geochim. Cosmochim. Acta, 46, 2363

Arnaud K. A., 1996, in Jacoby G. H., Barnes J., eds, ASP Conf. Ser. Vol. 101, Astronomical Data Analysis Software and Systems V. Astron. Sac. Pac., San Francisco, p. 17

Bałucińska-Church M., Belloni T., Church M. J., Hasinger G., 1995, A&A, 302, L5

Beloborodov A. M., 1998, ApJ, 496, L105

Beloborodov A. M., 1999, ApJ, 510, L123

Björnsson G., Svensson R., 1991, ApJ, 371, L69

Bolton C. T., 1972, Nat, 235, 271

Bowyer S., Byram E. T., Chubb T. A., Friedman M., 1965, Sci, 147, 394

Bregman J., Butler D., Kemper E., Koski A., Kraft R. P., Stone R. P. S., 1973, ApJ, 185, L117

Colpi M., 1988, ApJ, 326, 223

Coppi P. S., 1990, MNRAS, 258, 657

Coppi P. S., 1999, in Poutanen J., Svensson R., eds, ASP Conf. Ser. Vol. 161, High Energy Processes in Accreting Black Holes. Astron. Soc. Pac., San Francisco, p. 375

Coppi P. S., Blandford R. D., 1990, MNRAS, 245, 453

Cui W., Zhang S. N., Focke W., Swank J. H., 1997, ApJ, 484, 383

Cui W., Ebisawa K., Dotani T., Kubota A., 1998, ApJ, 493, L75 (C98)

Cunningham C. T., 1975, ApJ, 202, 788

Davis R., Hartmann L., 1983, ApJ, 270, 671

Di Matteo T., Blackman E. G., Fabian A. C., 1997, MNRAS, 291, L23

Dolan J. F., Tapia S., 1989, ApJ, 344, 830

Dolan J. F., Crannell C. J., Dennis B. R., Frost K. J., Orwig L. E., 1977, Nat, 267, 813

Done C., Życki P. T., 1999, MNRAS, 305, 457

Done C., Mulchaey J. S., Mushotzky R. F., Arnaud K. A., 1992, ApJ, 395, 275

Dotani T. et al., 1997, ApJ, 485, L87

Ebisawa K., Ueda Y., Inoue H., Tanaka Y., White N. E., 1996, ApJ, 467, 419

Esin A. A., McClintock J. E., Narayan R., 1997, ApJ, 489, 865

Esin A. A., Narayan R., Cui W., Grove J. E., Zhang S. N., 1998, ApJ, 505, 854

Fabian A. C., Rees M. J., Stella L., White N. E., 1989, MNRAS, 238, 729

Frankel N. E., Hines K. C., Dewar R. L., 1979, Phys. Rev. A, 20, 2120

Galeev A. A., Rosner R., Vaiana G. S., 1979, ApJ, 229, 318

Ghisellini G., Guilbert P. W., Svensson R., 1988, ApJ, 334, L5

Ghisellini G., George I. M., Fabian A. C., Done C., 1991, MNRAS, 248, 14

Ghisellini G., Haardt F., Svensson R., 1998, MNRAS, 297, 348

Gierliński M., Zdziarski A. A., Done C., Johnson W. N., Ebisawa K., Ueda Y., Haardt F., Phlips B. F., 1997a, MNRAS, 288, 958 (G97)

Gierliński M., Zdziarski A. A., Dotani T., Ebisawa K., Jahoda K., Johnson W. N., 1997b, in Dermer Ch. D., Strickman M. S., Kurfess J. D., eds, The 4th Compton Symposium. AIP, New York, p. 844

Gies D. R., Bolton C. T., 1982, ApJ, 260, 240

Gies D. R., Bolton C. T., 1986, ApJ, 304, 371

Gould R. J., 1975, ApJ, 196, 689

Haardt F., 1993, ApJ, 413, 680

Haardt F., Maraschi L., Ghisellini G., 1994, ApJ, 432, L95

Hanawa T., 1989, ApJ, 341, 948

Herrero A., Kudritzki R. P., Gabler R., Vilchez J. M., Gabler A., 1995, A&A, 297, 556

Holman G. D., Benka S. G., 1992, ApJ, 400, L79

Kaastra J. S., Mewe R., 1993, A&AS, 97, 443

Kato S., Fukue J., Mineshige S., 1998, Black-Hole Accretion Disks, Kyoto Univ. Press, Kyoto

Laurent P., Titarchuk L., 1999, ApJ, 511, 289

Liang E. P., Nolan P. L., 1984, Space Sci. Rev., 38, 353

Ling J. C. et al., 1997, ApJ, 484, 375

McConnell M. et al., 1994, ApJ, 424, 933

Magdziarz P., Zdziarski A. A., 1995, MNRAS, 273, 837

Malysheva L. K., 1997, Astron. Lett., 23, 585 [in Russian: AZh Pisma, 23, 667]

Margon B., Bowyer S., Stone R. P. S., 1973, ApJ, 185, L113

Massey P., Johnson K. E., DeGioia-Eastwood K., 1995, ApJ, 454, 171

Mises R., 1964, Mathematical Theory of Probability and Statistics, Academic Press, New York

Mitsuda K. et al., 1984, PASJ, 36, 741

Miyamoto S., Kimura K., Kitamoto S., Dotani T., Ebisawa K., 1991, ApJ, 383, 784

Morrison R., McCammon D., 1983, ApJ, 270, 119

Narayan R., Yi I., 1995, ApJ, 452, 710

Ninkov Z., Walker G. A. H., Yang S., 1987, ApJ, 321, 425

Ogawara Y., Mitsuda K., Masai K., Vallerga J. V., Cominsky L. R., Grunsfeld J. M., Kruper J. S., Ricker G. R., 1982, Nat, 295, 675

Paciesas W. S., Robinson C. R., McCollough M. L., Zhang S. N., Harmon B. A., Wilson C. A., , in, Dermer Ch.D., Strickman M. S., Kurfess J. D., 1997, The 4th Compton Symposium, AIP, New York, , p., 834

Paczyński B., Wiita P. K., 1980, A&A, 88, 23

Payne D. G., Blandford R. D., 1981, MNRAS, 196, 781

Phlips B. F. et al., 1996, ApJ, 465, 907

Poutanen J., 1999, in Abramowicz M., Björnsson G., Pringle J., eds, Theory of Black Hole Accretion Discs. Cambridge Univ. Press, Cambridge, p. 100

Poutanen J., Coppi P. S., 1998, Physica Scripta, T77, 57

Poutanen J., Svensson R., 1996, ApJ, 470, 249

Poutanen J., Krolik J. H., Ryde F., 1997, MNRAS, 292, L21

Press W. H., Teukolsky S. A., Vetterling W. T., Flannery B. P., 1992, Numerical Recipes, Cambridge Univ. Press, Cambridge

Reilman R. F., Manson S. T., 1979, ApJS, 40, 815

Ross R. R., Fabian A. C., 1993, MNRAS, 261, 74

Rybicki G. B., Lightman A. P., 1979, Radiative Processes in Astrophysics, Wiley-Interscience, New York

Shakura N. I., Sunyaev R. A., 1973, A&A, 24, 337

Shimura T., Takahara F., 1995, ApJ, 445, 780

Sowers J. W., Gies D. R., Bagnuolo W. G., Shafter A. W., Wiemker R., Wiggs M. S., 1998, ApJ, 505, 424

Stern B. E., Poutanen J., Svensson R., Sikora M., Begelman M. C., 1995, ApJ, 449, L13

Svensson R., 1999, in Poutanen J., Svensson R., eds, ASP Conf. Ser. Vol. 161, High Energy Processes in Accreting Black Holes. Astron. Soc. Pac., San Francisco, p. 361

Svensson R., Zdziarski A. A., 1994, ApJ, 436, 599 (SZ94)

Walborn N. R., 1973, ApJ, 179, L123

Webster B. L., Murdin P., 1972, Nat, 235, 37

Zdziarski A. A., 1998, MNRAS, 296, L51

Zdziarski A. A., Coppi P. S., Lamb D. Q., 1990, ApJ, 357, 149

Zdziarski A. A., Lightman A. P., Maciołek-Niedźwiecki A., 1993, ApJ, 414, L93

Zhang S. N., Cui W., Chen W., 1997a, ApJ, 482, L155

Zhang S. N., Cui W., Harmon B. A., Paciesas W. S., 1997b, in Dermer Ch. D., Strickman M. S., Kurfess J. D., eds, The 4th Compton Symposium. AIP, New York, p. 839

Zhang S. N., Cui W., Harmon B. A., Paciesas W. S., Remillard R. E., van Paradijs J., 1997c, ApJ, 477, L95

APPENDIX A: SPECTRUM FROM A PSEUDO-NEWTONIAN DISC WITH ZERO-STRESS INNER BOUNDARY

Let us consider a geometrically thin, optically thick, accretion disc around a Schwarzschild black hole with a mass M. We assume that the disc locally emits a blackbody spectrum, of which a fraction, p_{sc}, is then partly scattered in a corona. The unscattered flux observed from the disc is given by

$$F_\nu = (1 - p_{sc}) \frac{2\pi \cos i}{f_{col}^4 D^2} \int_{R_{in}}^{\infty} B_\nu(T) R \, dR, \tag{A1}$$

where B_ν is the blackbody spectrum. Other symbols used in this appendix are defined in Sections 1 and 3.1, except that we now drop subscripts in symbols for the colour temperature and mass. We allow here for truncation of the disc at $R_{in} \geq R_{ms} = 6GM/c^2$.

In order to compute the observed spectrum, we need to find the radial colour temperature distribution, $T(R)$. The rate of energy generation per unit area of one side of the disc, Q, is given by

$$Q(R) = -\frac{\dot{M}}{4\pi} \omega R \frac{d\omega}{dR} \left[1 - \frac{\omega(R_{ms}) R_{ms}^2}{\omega R^2} \right], \tag{A2}$$

where ω is the rotation velocity. The colour temperature is given by

$$qQ(R) = \sigma \left(\frac{T}{f_{col}} \right)^4, \tag{A3}$$

where σ is the Stefan–Boltzmann constant, and q is the ratio of the disc flux to $Q(R)$; see equation (B6) below. When a fraction (f) of $Q(R)$ is dissipated in a corona above the disc surface (SZ94), $q < 1$, and the disc emission is due to both internal dissipation of $(1 - f)Q(R)$ and irradiation by the corona. We adopt the pseudo-Newtonian potential (Paczyński & Wiita 1980),
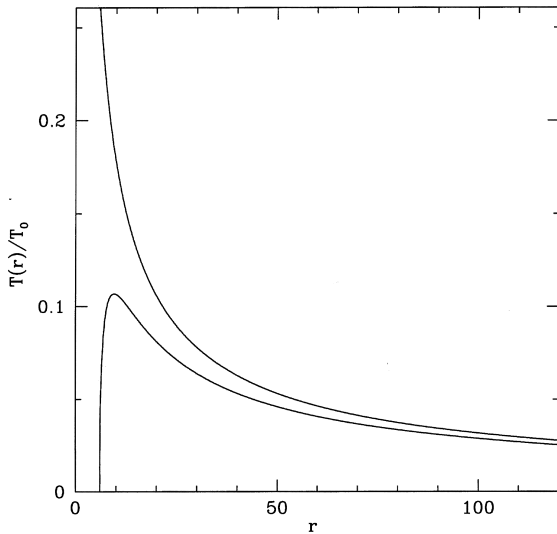
$$\Phi(R) = -\frac{GM}{R - 2R_g}. \tag{A4}$$

Figure A1. The radial temperature distribution in a pseudo-Newtonian disc, equation (A6) (lower curve), compared to the asymptotic distribution, $\propto r^{-3/4}$, used by the diskbb model (upper curve).

The rotation velocity is then

$$\omega(R) = \frac{1}{R - 2R_g} \left(\frac{GM}{R} \right)^{1/2}. \tag{A5}$$

Then we find from equations (A2) and (A3) that

$$T(r) = T_0 \left[\frac{r - 2/3}{r(r - 2)^3} \left(1 - \frac{3^{3/2}}{2^{1/2}} \frac{r - 2}{r^{3/2}} \right) \right]^{1/4}, \tag{A6}$$

where $r \equiv R/R_g$ and

$$T_0 = f_{col} \left(\frac{3\dot{M}qc^6}{8\pi\sigma G^2 M^2} \right)^{1/4}. \tag{A7}$$

At $r \gg 6$, $T(r) \simeq T_0 r^{-3/4}$. The maximum T is

$$T_{max} = \begin{cases} c_0 T_0, & r_{in} < r_{max}, \\ T(r_{in}), & \text{otherwise}, \end{cases} \tag{A8}$$

where $c_0 \simeq 0.1067$ and $r_{max} \approx 9.505$.

The (unscattered) flux emitted by the disc per unit photon energy, E, can be then obtained from equation (A1):

$$F_E = KE^3 \int_{r_{in}}^{\infty} \frac{r \, dr}{\exp[E/kT(r)] - 1}, \tag{A9}$$

where

$$K = (1 - p_{sc}) \frac{4\pi}{h^3 c^2} \left(\frac{GM}{c^2 D} \right)^2 \frac{\cos i}{f_{col}^4}, \tag{A10}$$

and h is the Planck constant. This model, under the name diskpn, is a part of the XSPEC package. Its parameters are T_{max}, r_{in} and the normalization K.

From these parameters, M can be obtained from equation (A10), and then $\dot{M}$ can be obtained using equations (A6)–(A8). For a constant K, $M \propto D f_{col}^2 \cos^{-1/2} i$. For constant K and T_{max}, $\dot{M} \propto D^2 f_{col} 4 \cos^{-1} i$. The disc luminosity is given by

$$L_s = \frac{2\pi D^2}{\cos i} \int F_E \, dE, \tag{A11}$$

which, for $r_{in} = 6$, equals

$$L_s = (1 - p_{sc}) q \frac{1}{16} \dot{M} c^2 = (1 - p_{sc}) \frac{\pi \sigma G^2 M^2 T_{max}^4}{6 c_0^4 f_{col}^4 c^4}. \tag{A12}$$

Finally, we point out that the above model differs significantly from a commonly used disc blackbody model, diskbb (Mitsuda et al. 1984) in XSPEC, in which the torque-free boundary condition is neglected and the asymptotic, $r \gg 6$, distribution is assumed, i.e., $T(r) = T_0 r^{-3/4}$. This is a sufficiently accurate model for $r_{in} \gg 6$. However, when the disc extends close to the minimum stable orbit, the discrepancy between this $T(r)$ and the $T(r)$ of equation (A6) becomes very significant, as shown on Fig. A1. Still, a diskbb spectrum can be made relatively accurate with some rescaling of R_{in} and T_{max}. We find in the case of $r_{in} = 6$ that a PN spectrum at some R_{in} and T_{max} is close to the diskbb spectrum computed for $R_{in}^{diskbb} \approx 2.73 R_{in}$ and $T_{max}^{diskbb} \approx 1.04 T_{max}$.

A more serious discrepancy regards the accretion efficiency. The efficiency ($\eta \equiv L/\dot{M}c^2$) of a PN disc extending to the minimum stable orbit is $\eta_{PN} = 1/16$, very close to the exact value in the Schwarzschild metric, $\eta_S = 1 - (8/9)^{1/2} \approx 0.0572$ (e.g. Kato, Fukue & Mineshige 1998), whereas the diskbb model

yields $\eta_{\text{diskbb}} = 1/4$. Therefore $\dot{M}$ for discs extending to the minimum stable orbit, computed using the `diskbb` model and assuming η_S (as is sometimes done), is 4.37 times less than the actual $\dot{M}$.

APPENDIX B: ENERGY BALANCE IN DISC-CORONA SYSTEMS

We express here energy balance between a corona and an underlying disc (see Fig. 6) in terms of the *observed* soft, hard and reflected fluxes, F_s, F_h and F_r, respectively. This allows a direct comparison with results of data fitting, in which we can distinguish between the flux in unscattered disc photons (F_s), the flux in scattered photons (F_h), and the flux in the unscattered Compton-reflection and Fe Kα photons (F_r).

We first note that F_s and F_h are related in different manners to the corresponding luminosities. The disc is optically thick, and thus it radiates with a semi-isotropic specific intensity, which implies $L_s = (2\pi/\cos i)D^2 F_s$. In general, the plasma emission can be anisotropic as well. If the emission radiated by the corona in directions away from the disc is isotropic (which we assume in this work), $L_h = 4\pi D^2 F_h$.

We then consider a corona dissipating a fraction, f, of the total available power, with the underlying disc dissipating the remaining $(1-f)$ fraction (SZ94). In general, the corona can be either homogeneous or patchy. In the latter case, L_s includes also emission of the part of the disc not covered by the corona. We will denote the powers dissipated in the corona and in the disc by P_c $(= fL)$ and P_d $[= (1-f)L]$, respectively. From energy conservation,

$$L = P_c + P_d = L_h + L_s + L_r. \tag{B1}$$

We will allow here for an anisotropic corona emission, in which the power emitted down equals d times the power emitted up. Also, we will include the power of Compton-reflected photons scattered in the corona in the total emission of the corona, $(1+d)L_h$. Thus the total emission of the corona includes its own dissipation and the power in photons emitted by the disc and then scattered,

$$(1+d)L_h = P_c + p_{sc}(P_d + dL_h), \tag{B2}$$

where p_{sc} is the average probability of scattering of a photon emitted by the disc. This can be solved for

$$L_h = \frac{P_c + p_{sc}P_d}{1 + d(1 - p_{sc})}. \tag{B3}$$

The luminosity in unscattered soft photons emitted by the disc includes parts due to the intrinsic disc emission and due to the re-emission of the incident coronal emission,

$$L_s = (1 - p_{sc})[P_d + d(1-a)L_h] \tag{B4}$$

(where a is the integrated albedo of the disc). The above equations can be solved for

$$L_s = \frac{(1 - p_{sc})\{[1 + d(1 - ap_{sc})]P_d + d(1-a)P_c\}}{1 + d(1 - p_{sc})}. \tag{B5}$$

The ratio of the soft flux at the disc surface to the total dissipation rate per unit area is

$$q = \frac{L_s}{(1 - p_{sc})L} \tag{B6}$$

(see Appendix A). Finally, the luminosity in unscattered Compton-reflected photons is

$$L_r = (1 - p_{sc})daL_h. \tag{B7}$$

The solution for f is

$$f = \frac{1 + d(1 - ap_{sc}) - p_{sc}(1 - p_{sc})^{-1}L_s/L_h}{1 + da(1 - p_{sc}) + L_s/L_h}. \tag{B8}$$

We note that our results are consistent with those of Poutanen & Svensson (1996). However, their condition of energy balance is expressed in terms of the total soft emission of the disc (denoted by l_s), which includes the part scattered in the corona, and the total emission of the corona (l_c), which includes the (unobserved) coronal emission directed towards the disc surface. For comparison with observations, those quantities need be transformed to the luminosities corresponding to observed fluxes; e.g., l_c corresponds to $(1+d)$ times the actual luminosity of the corona.

This paper has been typeset from a TEX/LATEX file prepared by the author.